Shock compression of liquid silicates to 125 GPa: The anorthite-diopside join

Paul D. Asimow[1] and Thomas J. Ahrens[1]

Received 17 November 2009; revised 8 June 2010; accepted 30 June 2010; published 26 October 2010.

[1] We determined the equation of state (EOS) of three silicate liquid compositions by shock compression of preheated samples up to 127 GPa. Diopside (Di; $Ca_2Mg_2SiO_6$) at 1773 K, anorthite (An; $CaAl_2Si_2O_8$) at 1923 K and the eutectic composition $Di_{64}An_{36}$ at 1673 K were previously studied by shock compression to 38 GPa. The new data extend the EOS of each composition nearly to the Earth's core-mantle boundary. The previously reported anomaly at 25 GPa for $Di_{64}An_{36}$ eutectic was not reproduced; rather all data for this composition fit within error a straight line Hugoniot in particle velocity vs. shock velocity. Di also displays a linear Hugoniot consistent with ultrasonic data and a third-order finite strain EOS. The full anorthite data set is complex; we examine a model with a transition between two structural states and a fourth-order finite strain model excluding two points that may not display relaxed behavior. We also report an experiment on room-temperature solid $Di_{64}An_{36}$ aggregate that clearly demonstrates increase upon compression of the Grüneisen parameter of this liquid, much as experiment and theory have shown for forsterite and enstatite liquids. We construct isentropes and isotherms from our Hugoniots using Mie-Grüneisen thermal pressure and evaluate the model of ideal mixing of volumes. Volume may mix almost linearly at high temperature, but deviates strongly when calculated along an isotherm; it remains difficult to reach a firm conclusion. We compare the densities of liquids to lower mantle solids. Our results suggest that basaltic liquids rich in CaO and Al_2O_3 are notably denser than liquids in the MgO-SiO_2 binary and, subject to uncertainties in the behavior of FeO and in corrections for thermal pressure, such liquids may be the most likely candidates for achieving negative buoyancy in the lowermost mantle.

Citation: Asimow, P. D., and T. J. Ahrens (2010), Shock compression of liquid silicates to 125 GPa: The anorthite-diopside join, *J. Geophys. Res.*, *115*, B10209, doi:10.1029/2009JB007145.

1. Introduction

[2] Silicate liquids play essential roles in the evolution and differentiation of terrestrial planets. The chemical fractionations associated with partial melting and crystallization processes generate compositional diversity among phases at small scale. The distinctive mobility of the liquid phase then leads to separation from the residue over large scales. This process generates chemically and isotopically differentiated reservoirs of planetary significance, including crusts and compositionally distinct mantle domains [*Albarede and Blichert-Toft*, 2007; *Allegre et al.*, 1995; *Elkins-Tanton et al.*, 2005; *Hutchison*, 1992; *Murthy*, 1992; *Shearer and Papike*, 1999]. Given the temperatures that occur in the current Earth, however, the stability field of liquid silicates is principally restricted to the upper ~100 km of the asthenosphere [*Hirschmann*, 2006]. Nonetheless, important reasons to study silicate liquids at substantially higher pressure have become clear in the decades since shock wave techniques were first applied to measuring the equation of state (EOS) of such liquids.

[3] First, seismic detection of ultra-low velocity zones (ULVZs) at the Earth's core-mantle boundary [*Garnero and Helmberger*, 1995; 1996; *Rost et al.*, 2005] support models wherein the thermal boundary layer at the base of the mantle reaches sufficiently high temperature to melt silicates [*Hernlund and Tackley*, 2007; *Lay et al.*, 2004]. Second, the likelihood of very large impact events during the early history of the Earth [*Morbidelli*, 2007] — notably but not exclusively the putative Moon-forming impact [*Canup*, 2004] — suggests in turn the likelihood of one or more deep magma ocean events [*Tonks and Melosh*, 1993], plausibly extending to the base of the mantle [*Labrosse et al.*, 2007].

[4] Understanding the physical and chemical causes and consequences of deep mantle melting requires a range of experimental data, including phase equilibria, trace element partition coefficients, transport properties such as viscosity and diffusivity, and equations of state for solid and liquid

[1]Division of Geological and Planetary Sciences, California Institute of Technology, Pasadena, California, USA.

0148-0227/10/2009JB007145

phases. This study focuses on the EOS — i.e., the functional relationship among density (ρ), pressure (P), temperature (T) and composition — of silicate liquids. Liquid density and its dependence on P, T, and composition are particularly fundamental for at least two distinct reasons. First, gravity-driven differentiation depends on the magnitude and sign of crystal-liquid density differences [*Agee*, 1998; *Ohtani et al.*, 1995; *Stolper et al.*, 1981]. Second, the reciprocal of density, specific volume (V), is a thermodynamic variable that defines the pressure dependence of specific Gibbs free energy and hence the shift of equilibria with increasing P; an accurate EOS is one prerequisite for useful thermodynamic models of mantle melting [*Ghiorso*, 2004b].

[5] Silicate liquid EOS data are obtained from a range of experimental techniques including direct Archimedean buoyancy measurements and ultrasonic sound speed during ambient pressure heating [*Ai and Lange*, 2008; *Lange*, 1997] and sink-float experiments in static compression piston-cylinder and multi-anvil devices [*Agee*, 2008; *Suzuki et al.*, 1998]. The sink-float method can be carried out with hydrous or carbonated melts, and has recently been applied to the possibility of dense volatile-rich melts at 410 km depth in the mantle [*Ghosh et al.*, 2007; *Matsukage et al.*, 2005; *Sakamaki et al.*, 2006]. A variety of other experimental methods – including in situ ultrasonic interferometry, computed X-ray tomography, radiographic X-ray contrast imaging [*Sakamaki et al.*, 2009; 2010], and diffuse X-ray scattering – have recently been demonstrated to measure density or sound speed in liquids at high pressure but application to silicate liquids is in its infancy. Increasingly, computational methods are also able to define the EOS of silicate liquids at high pressure, either through empirical molecular dynamics on large systems ($\sim 10^4$ atoms) [*Adjaoud et al.*, 2008; *Ghiorso et al.*, 2009; *Spera et al.*, 2009] or *ab initio* molecular dynamics applied to smaller systems ($\sim 10^2$ atoms) [*Karki et al.*, 2006].

[6] Shock wave experiments can also be used to determine the EOS and melting points of silicate systems in several ways. First, even when the starting material is a room-temperature solid, shock compression involves substantial temperature increase and a strong enough shock will drive the material into a molten state, with a phase transition occurring during passage of the shock wave [*Luo and Ahrens*, 2004; *Lyzenga et al.*, 1983]. The family of states achieved by increasingly strong shock compression from a given initial state is called a Hugoniot, and the occurrence of melting along Hugoniots can be recognized by discontinuities in the pressure-density curve [e.g., *Akins and Ahrens*, 2002], drops in shock temperature [e.g., *Williams et al.*, 1987], or drops in the velocity of rarefaction fronts traveling in shocked material [e.g., *Hixson et al.*, 1989]. Shock states along initially solid Hugoniots that are determined to have achieved melting can then constrain the EOS of the melt [e.g., *Mosenfelder et al.*, 2007; *Mosenfelder et al.*, 2009]. However, this approach is indirect, depending on the identification of shock melting and requiring as input the enthalpy of the melting transition.

[7] A more direct approach is to pre-heat the target material above its ambient-pressure melting point before shock compression. Previous work of this kind has extended to a maximum pressure of 40 GPa [*Chen et al.*, 2002; *Miller et al.*, 1991; *Rigden et al.*, 1984; *Rigden et al.*, 1988; 1989; *Rowan*, 1993]. In this case, even though the Hugoniot may pass below the liquidus for a short interval at low pressure, there is expected to be insufficient time to crystallize the liquid, such that shock compression samples the liquid state at all pressures [*Rigden et al.*, 1988]. Furthermore, the timescale of shock compression is comparable to or longer than the structural relaxation time of silicate liquids at the shock temperature [*Rigden et al.*, 1988]. This implies that shock compression can accurately characterize the zero-frequency, relaxed, or static elastic moduli of liquids and the resulting EOS can be used to predict static liquid (as opposed to unrelaxed or glass-like) behavior. The strongest evidence for this is that the intercepts of the resulting Hugoniots are consistent, within error, with independently measured zero-pressure bulk sound speeds in the same liquids, where relaxation can be established by demonstrating an absence of dispersion [*Ai and Lange*, 2008]. There is an intermediate pressure range where unrelaxed behavior is possible and, in fact, two of the Anorthite liquid experiments of *Rigden et al.* [1989] have been questioned on just this basis [*de Koker*, 2010; *Ghiorso et al.*, 2009]. We consider below the consequences of including or excluding these data in fits of the total data set. For the much stronger shocks and much higher shock temperatures obtained in this work, we expect that relaxation will be still less of an issue; the rise time of strong shocks is comparable to the weaker shocks previously studied, but the relaxation times of the melts should be much shorter.

[8] Section 2 of this paper documents our experimental methods. Section 3 reports new data on diopside (Di), anorthite (An), and diopside-anorthite eutectic ($Di_{64}An_{36}$) liquids up to 125 GPa, obtained by extending experimental techniques previously developed for the Caltech 40 mm single-stage gun to the Caltech 25 mm two-stage light-gas gun. New data reductions of previous experiments on the same compositions are reported for consistency in the overall dataset. In addition, we report one experiment that drove a room-temperature solid $Di_{64}An_{36}$ target into the shock-melting regime, for comparison to the pre-heated liquid Hugoniot of the same composition. Fitting of these data to straight lines in shock velocity (U_s) vs. particle velocity (u_p) space by unweighted linear regression is included in Section 3. Section 4 describes analysis using weighted chi-squared fitting of the shock wave data together with constraints on the ambient pressure density and sound speed to obtain thermal EOS fits independently for each composition. Section 5 uses all three compositions together to assess the degree to which linear mixing of molar volumes is valid and to discuss general implications for the properties of silicate liquids at lower mantle conditions and the compositions of liquids that might occur in a ULVZ at the core-mantle boundary.

2. Experimental Methods

[9] The experimental techniques here are descended from the methods originally developed by *Rigden et al.* [1984] and successively refined and extended by *Rigden et al.* [1988; 1989], *Miller et al.* [1988; 1991], *Chen et al.* [1998; 2002] and *Asimow et al.* [2008].

Table 1. Sample Compositions

	Anorthite			Diopside			Di64An36		
	nominal	average	S.D.[a]	nominal	average	S.D.[a]	nominal	average	S.D.[a]
SiO_2	43.194	42.686	0.198	55.492	55.216	0.134	50.333	49.844	0.148
TiO_2	0	bd[b]		0	bd[b]		0	bd[b]	
Al_2O_3	36.649	36.394	0.094	0	0.190	0.010	15.374	15.356	0.069
Cr_2O_3	0	bd[b]		0	bd[b]		0	bd[b]	
FeO	0	0.041	0.012	0	0.027	0.019	0	0.018	0.016
MnO	0	bd[b]		0	bd[b]		0	bd[b]	
MgO	0	0.166	0.003	18.612	18.034	0.060	10.804	10.507	0.041
CaO	20.157	20.232	0.046	25.896	26.256	0.050	23.489	23.811	0.035
Na_2O	0	0.018	0.011	0	0.079	0.008	0	0.067	0.021
K_2O	0	0.017	0.009	0	bd[b]		0	0.010	0.008
Total	100	99.559	0.209	100	99.823	0.195	100	99.623	0.159

[a]S.D. = 1 standard deviation.
[b]bd = below detection limit.

2.1. Sample Preparation

[10] Four samples were used in this study: glass of diopside composition, glass of anorthite composition, glass of 64 mol% diopside plus 36 mol% anorthite, and a polycrystalline diopside+anorthite solid aggregate of the same composition. The samples were obtained as follows.

[11] Diopside glass was synthesized as small beads and fibers by spin quench at Dow Corning Corporation. The stoichiometry was verified by crystallization to single-phase diopside by *Baxter et al.* [2007]. We fused this glass in 10 g batches for at least 6 hours at 1773 K in Au-Pt crucibles under vacuum, and quenched by removing from the furnace to air; this yields a bubble-free, crack-free, crystal-free mass of glass. The glass was annealed at 773 K overnight to relax thermal stresses before core drilling to extract disks 2.5 mm thick and 8 mm in diameter.

[12] Anorthite glass is from a large wafer also manufactured by Dow Corning, but made by pouring liquid onto a cold plate. An glass disks were simply cored directly from the wafer.

[13] $Di_{64}An_{36}$ glass was prepared by powdering the Di and An glasses in a steel percussion mortar, magnetically removing steel fragments, drying the powders overnight at 383 K, and then weighing the appropriate proportions of each powder. They were combined in an agate mortar and ground under ethanol for 30 minutes before fusing in vacuum at 1673 K for 24 hours. The sample was quenched in air, powdered, reground, and fused a second time. It was annealed and cored as with the diopside glass.

[14] Finally, a 10 g sample of $Di_{64}An_{36}$ glass was crystallized in air using the following time-temperature schedule: 24 hours above the liquidus at 1673 K, followed by a step to a 6 hour dwell at 1523 K, a ramp at 100 K/hr to 1373 K, and finally air quench, yielding a fine-grained fully crystalline diopside-anorthite aggregate (microtexture and phases were confirmed by scanning electron microscopy).

[15] Electron probe analyses of the diopside, anorthite, and $Di_{64}An_{36}$ glasses (CIT JEOL 8200 probe, mineral and oxide standards, 15 kV, 10 nA, 10 μm beam) are shown in Table 1.

2.2. Encapsulation and Measurement

[16] Each glass disk was welded into a Mo container as follows. Specification ABL4 Mo (>99.97% pure, H. C. Starck Co.) rods of 1.75″ and 0.5″ diameter were machined into a driver-capsule assembly and a sample cap (see schematic in Figure 1a). The driver-capsule piece was a disk 2.25 mm thick and 44.5 mm in diameter with a cylindrical projection on one side, with outer diameter 10 mm and inner diameter 8 mm. The projection was 3.25 mm high, but a shoulder with outer diameter 9 mm and depth 0.75 mm was cut into the end of it. The sample cap was a disk 9 mm in diameter and 0.75 mm thick. The cap is attached using

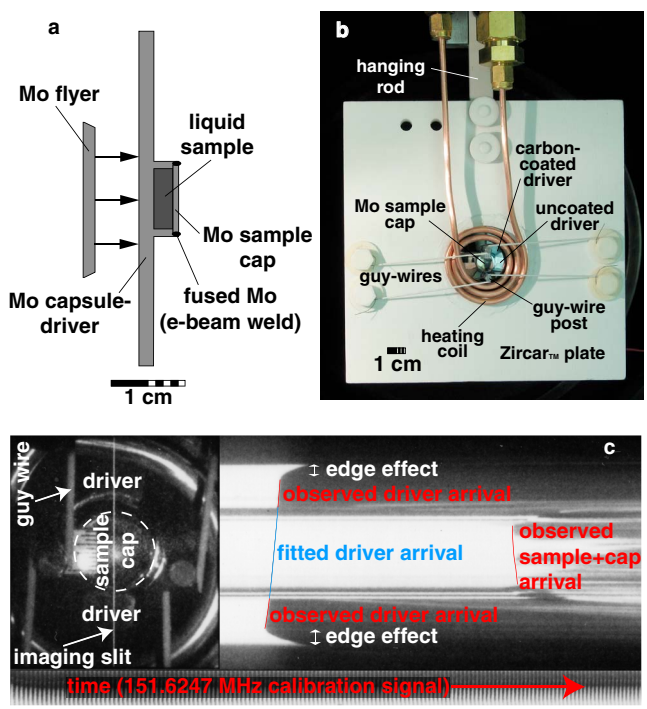

Figure 1. Illustration of the experimental configuration. (a) Cross-section of the sample capsule assembly; note 1 cm scale bar. (b) Photograph of target assembly, looking up-range; key parts are labeled. (c) Example streak record (shot 364). The static photograph of target taken with streak camera indicates the location of driver and sample cap reflections; the divisions of the ruler scale visible in this image are 1 mm. The calibration record indicates the time scale. Key events on the streak record are indicated.

Table 2. Shock Compression Data

	Shot #	Flyer	T (K)	U_{fp} km s^{-1}	±	u_p km s^{-1}	±	U_s km s^{-1}	±	ρ kg m^{-3}	±	P (GPa)	±
Anorthite													
Rigden et al. [1989]	666	Cu	1919.6	1.24	0.03	0.920	0.020	3.98	0.05	3.33	0.03	9.4	0.3
(revised)	673	Cu	1919.4	1.3	0.02	0.969	0.020	3.94	0.02	3.40	0.02	9.8	0.2
	664	Cu	1922.2	1.52	0.03	1.133	0.023	4.12	0.08	3.54	0.04	12.0	0.4
	665	Cu	1922.2	1.8	0.03	1.325	0.025	4.68	0.01	3.57	0.03	15.9	0.3
	663	W	1902.7	2.03	0.04	1.960	0.040	5.32	0.02	4.06	0.05	26.7	0.5
	672	W	1924.2	2.49	0.03	2.363	0.005	5.88	0.06	4.29	0.04	35.6	0.3
This work	LGG364	Mo	1930	4.997	0.005	3.802	0.015	8.64	0.16	4.57	0.08	83.9	1.2
	LGG380	Mo	1932	5.434	0.003	4.094	0.007	9.09	0.08	4.66	0.04	95.3	0.6
	LGG379	Mo	1932	6.007	0.025	4.488	0.016	9.70	0.16	4.77	0.08	111.5	1.4
	LGG382	Mo	1932	6.533	0.013	4.868	0.024	10.06	0.23	4.97	0.13	125.5	2.3
Diopside													
Rigden et al. [1989]	660	Cu	1771.5	1.03	0.03	0.739	0.020	4.47	0.01	3.14	0.02	8.7	0.3
(revised)	656	Cu	1772.3	1.50	0.03	1.076	0.030	4.92	0.01	3.36	0.02	13.9	0.3
	629	Cu	1717.6	1.55	0.04	1.119	0.030	4.80	0.09	3.42	0.04	14.1	0.5
	630	Cu	1448.4	2.00	0.04	1.414	0.030	5.79	0.12	3.47	0.03	21.5	0.5
	658	W	1503.5	2.12	0.04	1.960	0.040	6.39	0.05	3.79	0.03	32.8	0.6
	659	W	1499.9	2.42	0.04	2.237	0.040	6.51	0.05	4.00	0.04	38.2	0.6
	655	W	1498.8	2.46	0.03	2.265	0.030	6.61	0.08	3.99	0.03	39.3	0.6
This work	LGG363	Mo	1508	4.984	0.003	3.763	+0.032	8.58	+0.35	4.67	+0.09	84.7	+2.7
							−0.016		−0.17		−0.17		−1.3
	LGG378	Mo	1508	5.957	0.003	4.403	0.002	9.89	0.02	4.73	0.01	114.3	0.2
Di64An36													
Rigden et al. [1988]	592	Al	1379.0	1.05	0.03	0.446	0.020	3.87	0.06	2.96	0.01	4.5	0.2
(revised)	593	Al	1390.0	1.5	0.02	0.651	0.010	3.94	0.06	3.14	0.02	6.7	0.2
	605	Al	1397.0	2	0.05	0.873	0.024	4.38	+0.08	3.27	+0.04	10.0	+0.3
									−0.13		−0.03		−0.3
	606	Mo	1387.0	1.5	0.025	1.232	0.020	4.83	+0.12	3.52	+0.14	15.6	+0.3
									−0.42		−0.03		−1.1
	627	Cu	1404.6	1.69	0.03	1.219	0.023	4.95	+0.12	3.47	+0.04	15.8	+0.3
									−0.15		−0.03		−0.4
	607	W	1390.0	1.8	0.04	1.722	0.040	5.37	0.01	3.85	0.04	24.2	0.5
	654	W	1404.2	2.04	0.05	1.924	0.050	5.82	+0.18	3.91	+0.05	29.3	+0.7
									−0.13		−0.07		−0.7
	628	W	1398.7	2.22	0.05	2.067	0.050	6.24	0.01	3.91	0.05	33.8	0.8
This work	1061	W	1400	2.64	0.02	2.429	0.003	6.50	0.05	4.17	0.01	41.3	0.5
	LGG357	Mo	1405	4.951	0.008	3.716	0.004	8.83	0.05	4.51	0.02	85.8	0.3
	LGG361	Mo	1403	5.882	0.003	4.385	0.003	9.57	0.03	4.83	0.02	109.9	0.3
	LGG381	Mo	1406	6.459	0.009	4.763	0.004	10.23	0.04	4.90	0.02	127.5	0.4
Di64An36 solid aggregate													
	LGG368	Mo	300	6.31	0.01	4.212	0.016	10.29	0.10	5.21	0.04	133.4	1.0

electron-beam welding, yielding a sealed cylindrical sample cavity 8 mm in diameter and 2.5 mm thick. The impact face of the driver was ground to 6×10^{-6} inch finish. The rear face, both inside the cylindrical capsule and outside, was polished to mirror finish using diamond pastes down to 1 μm. The final polished shape of the driver was characterized by measuring a line profile of heights (z-coordinate, or direction of shock propagation) with a needle-tip depth micrometer with 1 μm resolution, as the sample was stepped in 100 μm increments along the horizontal direction (x-coordinate, i.e. along the imaging slit of the streak camera) using a digital mill table.

[17] For experiments up through LGG361 (sequential shot numbers are given in Table 2), the sample caps were fine-polished on the inside only before welding; the outer surface was fine-polished after welding, taking care not to damage the weld but resulting in some uncertainty in the thickness of the cap after polishing. For the last eight experiments reported, the sample caps were fine-polished on both sides before welding so that the final cap thickness is well known. The volume of glass to be loaded in each capsule was estimated from knowledge of the thermal expansion of Mo and the thermal expansion and volume of fusion of the sample, the intent being to slightly underfill the capsule at the run temperature. This avoids bowing of the cap from overpressure and allows a small void bubble that rises to the top, out of the plane of the experiment. The detailed final shape of the capsule exterior was then measured with three parallel profiles 250 μm apart in the y-direction (to check for tilt perpendicular to the slit) across the top of the sample cap as described above.

[18] Each capsule was leak-checked by heating to the intended run temperature in a vacuum tank for several minutes. Surface oxidation that occurred during heat testing was gently polished off without significant change in the exterior dimensions of the capsule.

[19] The crystalline aggregate was not encapsulated. It was simply cut and polished to make a rectangular plate 4.8 × 4.2 mm across and 0.91 mm thick, which was glued to a Ta driver plate with glass mirrors, alongside a perovskite + majorite specimen as described in *Mosenfelder et al.* [2009].

2.3. Shock Wave Loading

[20] Figure 1b shows a capsule prepared for loading as follows. Each Mo capsule assembly was coated with amorphous carbon everywhere except for the reflecting

region imaged by the streak camera slit, which was masked during coating (Cressington model 208C coater). Coating continued up to thicknesses of ~90 and ~110 nm on the up- and down-range surfaces. The carbon coating provides an oxygen getter to reduce oxidation of the reflecting surface during heating. The capsule was then attached to a Zircar™ ZAL-45 alumina fiber insulation rigid plate and held in place by a "guy-wire" assembly consisting of two Mo posts extending from the back of the driver, with W-Re alloy wire passing through holes at the end of the posts and anchored to the ceramic plate with alumina screws. The ceramic plate was attached by a 0.5″ × 0.25″ × 6″ Macor™ bar to a brass block clamped onto the outer 1″ diameter Cu cylinder of a vacuum-sealed coaxial support rod whose inner and outer cylinders were connected to the two terminals of the final transformer (Lepel model LCT-4) of a Lepel 10 kW radio frequency (RF) generator. The brass block also provided the attachment point for both ends of a Cu-tube induction coil [*Chen and Ahrens*, 1998] and cooling water inlet and outlet ports.

[21] Samples were heated by coupling of RF currents from the coil to the capsule assembly. Temperature was monitored using a Williamson Corp. model 8210S-C-T two-color pyrometer operating at 0.71 and 0.81 μm. The pyrometer was calibrated, for our particular combinations of mirrors and viewing windows, against a type S Pt-Rh thermocouple. All samples were stable at the reported temperature ±1 K for tens of seconds before firing. About one second before firing, a turning mirror was extended. The mirror blocks the pyrometer view and instead forms a light path [for schematic, see Figure 6 of *Chen et al.*, 2002] from a Xe flash lamp (EG&G model FX-42C-2) to the back of the target, with reflected light reflecting again from the turning mirror and into a Hadland Imacon 790 streak camera equipped with a 25 μm slit (Nikon ED 70–300mm f4–f5.6 zoom lens with 2 or 3 Nikon PK13 extension tubes, 27.5mm length each, for image magnification of ~0.7 to ~0.9). Streaks of 1500 ns duration provide time resolution for sharp cutoffs of ~0.2 ns. Time on the streak was calibrated using a 151.6247 MHz radio oscillator connected to the grids of the image converter (the calibration streak is shown alongside an experiment record in Figure 1c); this periodic signal allowed correction for non-linearity of the streak rate.

[22] All the new Mo-capsule experiments reported here were impacted by Mo flyer plates. In one experiment (1061), the projectile was launched by the Caltech single-stage 40-mm bore propellant gun. Flyer velocity on this gun is determined redundantly by three laser-interrupts and a double-flash X-ray system with estimated velocity uncertainty of 1% [e.g., *Chen et al.*, 2002]. The streak camera was triggered by impact pins specially manufactured from Al_2O_3 and Ta parts such that they would function and maintain an open circuit at 1673 K.

[23] All the remaining experiments were performed in the Caltech 25 mm two-stage light gas gun. Flyer velocity was determined redundantly by two systems, as described in *Asimow et al.* [2008]: a double-flash X-ray system with estimated precision of ±0.2% (e.g., ±12 m/s at 6000 m/s) and a two-magnet induction detector [*Hawke et al.*, 1995] with estimated precision of ±0.1%. In all cases the two measurements agree to within the stated uncertainty; we use the average of the two measurements, but 0.2% uncertainty in flyer velocity has negligible effect on the uncertainty of the derived data. The two velocity magnets also provided up-range trigger signals that were used to forecast the impact time, with a first-order correction for pre-shot uncertainty in flyer velocity. The first magnet signal triggered the X-ray flash delay generator and the xenon flash lamp that provided illumination for streak camera imaging. The magnet signals were converted to TTL pulses and used to trigger the start and stop inputs of a 50 MHz up-down counter. The up-down counter is programmed with the measured distance from magnet 1 to 2 (~200 mm) and a fictive distance adjusted from the measured distance from magnet 2 to target (true distance also ~200 mm), such that the output pulse from the end of the down-count triggered the streak camera so as to place the streak cutoffs near the center of the streak. Accounting for all cable and intrinsic delays in the system, this non-contact triggering system is able to start the camera at the appropriate time relative to impact with reproducibility ≤25 ns, even though the first magnet crossing is 60–80 μs before impact.

2.4. Data Reduction

[24] Inputs to the data reduction are the flyer velocity; streak duration; driver, sample and cap thickness profiles; and initial temperature. These are analyzed together with reference data as follows. The initial density and Hugoniot parameters (C_o and s) of the flyer material, cold Mo; the thermal expansion function of Mo, used to correct sample and capsule thicknesses and to obtain the initial density of the pre-heated Mo driver and cap; and the Hugoniot parameters of hot Mo as functions of temperature were all critically evaluated and reviewed in *Asimow et al.* [2008]. The initial densities of the sample liquids as functions of temperature are from *Lange* [1997].

[25] The streak image is digitized at 2400 dpi and 8 bit grayscale and rotated so that the time direction is parallel to an axis of the image raster (see Figure 1c). A quadratic pixel vs. time function is derived from the calibration streak. Driver and sample cutoffs usually manifest as sharp decreases in brightness and are chosen as the first pixel along a time-line whose brightness is at least 15 gray levels (out of 256) darker than the average of the previous 50 pixels. In some cases, cutoffs manifest as a sharp increase in brightness due to blown-off gases; such cutoffs were also picked using a 15 grey-level threshold to avoid false picks due to pixel noise. This picking algorithm typically yields several hundred points on the driver cutoff, in two groups on either side of the sample capsule, and several hundred points across the cap of the sample chamber itself. The position of these picks in the x-direction across the capsule assembly is co-registered with the line profiles of driver, sample, and cap thickness previously measured by micrometer and digital mill table.

[26] The time of shock entry into the sample at each point across the capsule is estimated as follows. The shape and time of the shock wave in the driver is derived by correcting each driver arrival pick from the thickness z of the actual reflecting surface to a common thickness datum. This calculation requires the shock velocity in the driver, obtained by impedance match using the measured flyer velocity and the shock properties of the cold Mo flyer and hot Mo driver. After excluding points affected by proximity to the edge of

the flyer, the resulting set of (x, time) pairs are then fitted to a polynomial in x in order to calculate the time of shock arrival across the driver surface inside the capsule, which cannot be observed directly. Fourth-order polynomials were found to represent the shock front shape, accounting for flyer tilt and bowing. Much of the uncertainty in shock velocity is derived from uncertainty in this interpolation. Finally, for each point across the streak where a cap cutoff determination could be made, the time of shock entry into the liquid sample is obtained by again correcting the fitted shape and time of the shock from the constant-thickness datum to the measured z-height of the inside driver at that x-point. The liquid sample and Mo cap thicknesses at each x-point are also estimated by interpolation of the line-profiles across the cap after welding and polishing. Here two different approaches were used. For shots up to LGG361, where the cap was polished after welding, it was assumed that the inside surface of the cap was a straight line along x and was in direct contact with the shoulder at the measured heights of the shoulder on either side. Remaining relief in the measured profile (typically $\leq$75 μm) was then attributed to variations in cap thickness due to polishing. For shots after LGG361, the cap was pre-polished and its thickness precisely known; in this case topography in the measured profile (typically $\leq$40 μm) was assigned to variations in sample thickness, allowing that contact between the cap and the shoulder might not be perfect and that some bowing of the cap might occur during welding or pre-heating.

[27] Finally, the iterative solution for shock states and travel times in the sample and cap as described by *Rigden et al.* [1988] was carried out independently at each pixel across the x-direction of the streak where cap cutoff measurements could be obtained. To be clear, this calculation takes as input a series of parameters that are constants across the streak (shock and particle velocity in the driver, the initial sample density at the measured temperature, and the Hugoniot properties of the hot Mo) as well as some that are functions of position x across the streak (the thicknesses of sample and cap, the time of shock entry to the sample as obtained above and the time of shock breakout from the cap). The result is a family of solutions for Hugioniot pressure (P_H), shock velocity (U_s), particle velocity (u_p), and Hugoniot density (ρ_H) in the sample. The final uncertainty is dominated by the distribution of these individual solutions. The uncertainty in the input parameters, which impart systematic error to each point in the distribution, are typically negligible compared to the random error from irregular driver and sample cutoffs on the streak image. However, the complete error analysis reflects both propagation of uncertainties in the reference data and the spread of the population of pixel-line by pixel-line shock state determinations.

2.5. Re-Analysis

[28] We re-analyzed the original shot records from experiments reported in *Rigden et al.* [1988; 1989] and a few shots carried out by Rigden and co-workers that were not included in publications. We went back to the original streak camera images, re-measured shock travel times, and carried out the full analysis described above. Consistency of the overall dataset was maintained by using the new reference properties of hot Mo [*Asimow et al.*, 2008] and initial sample densities [*Lange*, 1997].

[29] Differences between the original and revised values for the Hugoniot parameters of most shots are within stated uncertainties, except for two discrepant shots that have little overall influence on the fitted equations of state. Both the original and revised data are shown in the following figures along with new data.

3. Results

[30] Experimental data are reported in Table 2. Each experiment is assigned a shot number and described by sample material; initial temperature; flyer standard material; flyer velocity u_{fp} with uncertainty; and the derived parameters u_p, U_s, ρ_H and P_H with the associated uncertainty for each. The uncertainty in each derived parameter is obtained from adding in quadrature the analytical errors propagated from uncertainty in all standard parameters [*Jackson and Ahrens*, 1979; *Mosenfelder et al.*, 2007] together with the empirically observed variance in the derived quantities across each streak record. In most cases both sources of error are treated as Gaussian. However, in a few cases the distribution of travel times observed is highly skewed. For these experiments we report asymmetrical errors obtained from the 10th and 90th percentiles of the data distribution.

3.1. Diopside-Anorthite Eutectic Liquid

[31] The data for $Di_{64}An_{36}$ liquid are shown in Figure 2. The seven experiments on this composition of *Rigden et al.* [1988] are all reproduced within about one overlapping standard deviation (that is, given original parameter and uncertainty $x_1 \pm \sigma_1$ and revised estimate $x_2 \pm \sigma_2$, we obtain $|x_1 - x_2|/(\sigma_1 + \sigma_2) \leq 1$) in all derived parameters by the re-analysis. There is no evident systematic bias from the revisions in standard properties. In addition, experiment 606 (Mo flyer at 1.5 km s^{-1}), which was carried out but not reported by Rigden et al. due to high tilt of the projectile and dim illumination of the streak record, turns out to be a near-duplicate of shot 627 (Cu flyer at 1.69 km s^{-1}) and is fully consistent with the trend of the original data. There are four new preheated liquid experiments on this composition: one 40 mm single stage gun experiment and three light gas gun experiments. The driver and sample cut-offs observed in all four of the new experiments are sharp and well defined, with a narrow dispersion in travel times yielding good precision in all the new data, with shock velocity uncertainties $\leq$90 m s^{-1} and pressure uncertainties $\leq$0.7 GPa.

[32] These data are very well fit using simple unweighted linear regression by a straight line in U_s-u_p space, with intercept C_o = 2993 ± 75 m s^{-1}, slope s = 1.52 ± 0.03, and correlation coefficient r^2 = 0.996. The intercept of this fit is consistent, within mutual errors, with the ambient pressure, 1673 K sound speed in this liquid, 2963 ± 20 m s^{-1}, from *Ai and Lange* [2008]. Given the high precision of the ultrasonic velocity, our preferred Hugoniot for this composition has C_o fixed to 2963 m s^{-1}, in which case the best-fit value of s = 1.534 ± 0.016, r^2 = 0.999. The intercept is also consistent, within error, with the low-pressure segment of the piecewise-linear Hugoniot of Rigden et al. (C_o = 3060 m s^{-1}), but the slope of the low-pressure segment that Rigden et al. fit only to the first six data points is significantly lower (s = 1.36). As we will discuss below, the higher value of s in the new fit is consistent with the value for the isentropic

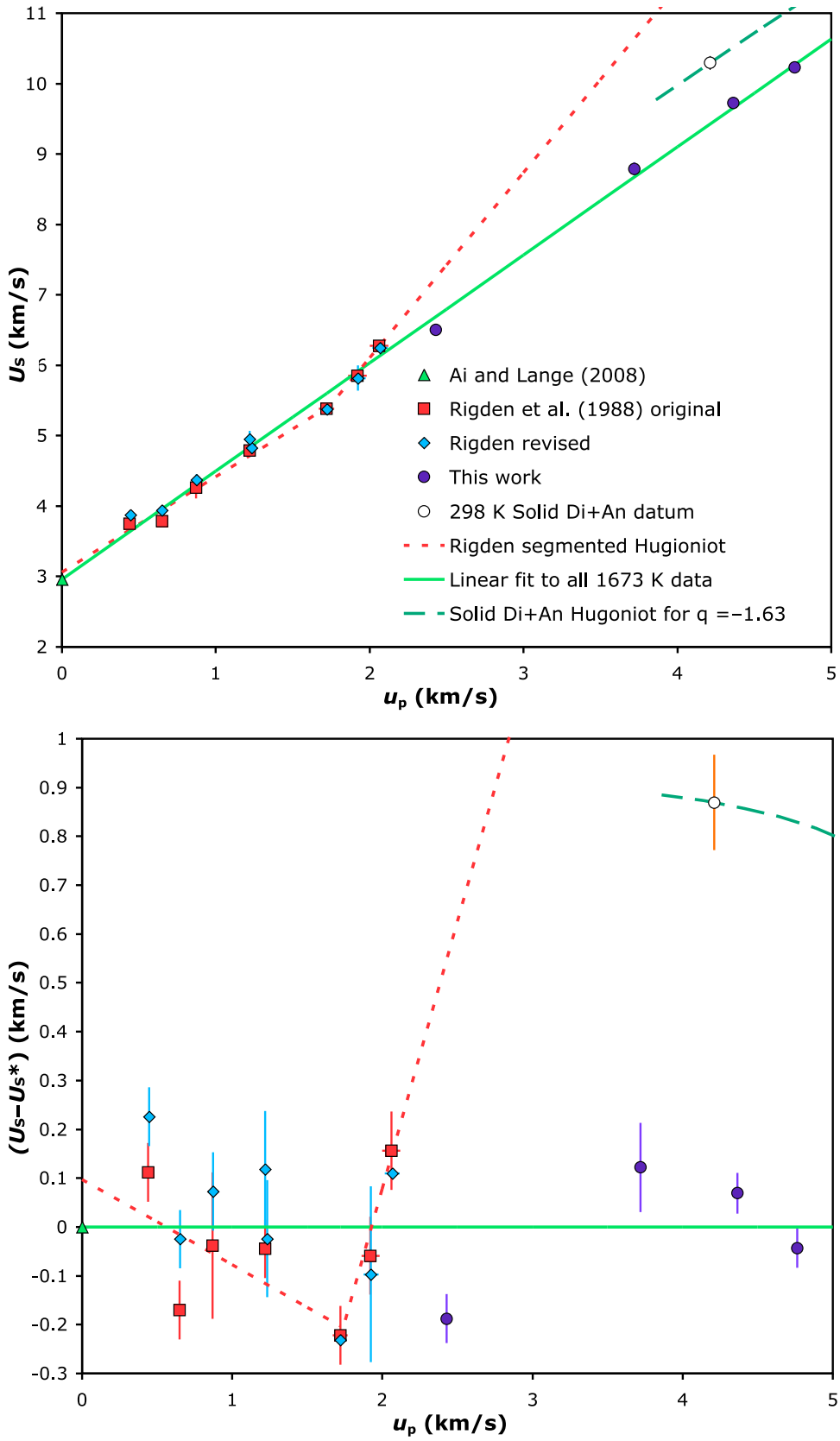

Figure 2. Hugoniot data for $Di_{64}An_{36}$ liquid preheated to ~1673 K. (a) Shock velocity (U_s) vs. particle velocity (u_p). (b) Same data and models plotted as reduced shock velocity U_s-U_s*, where U_s* = 2963 + 1.534 u_p m s^{-1} is the best fitting line to the whole data set. Error bars shown are 1 standard deviation.

pressure derivative of the isentropic bulk modulus, K'_S (5.35, similar to the value of 5.6 derived by *Ai and Lange* [2008] but higher than the value of 4.85 reported by *Rigden et al.* [1988]) that results from our fitting to a Birch-Murnaghan/Mie-Grüneisen EOS.

[33] The good linear fit to the entire data set for this composition is surprising insofar as *Rigden et al.* [1988] concluded that their two highest pressure points defined anomalous compression, with a sharp kink in the Hugoniot at u_p = 1.72 km s^{-1}. With data now extending to u_p = 4.76 km s^{-1}, it is clear that this Hugoniot does not have a sharp kink as suggested by *Rigden et al.* [1988] and that this liquid remains compressible beyond 24 GPa. The apparent kink is the previous data set is now seen to have been an unfortunate result of normal scatter of a small number of data points. We discuss below the consequences of the continued compressibility of this material for compression mechanisms of silicate liquids and for the buoyancy of basaltic liquids in general, relative to lower mantle minerals.

3.2. Diopside

[34] The data for Di liquid is shown in Figure 3. The re-analysis reproduces most of the five experiments on this liquid from *Rigden et al.* [1989] within one overlapping standard deviation, but there are some discrepancies. In particular, despite repeated examination of the shot record for experiment 630 (Cu flyer at 2.0 km s^{-1}), we were unable to obtain a travel time comparable to that reported by Rigden et al.; this shot becomes an outlier, impossible to fit within error by a straight line Hugoniot or by any of the EOS formalisms considered below. The anomalous behavior may be related to initial temperature, which is ~50 K lower for this shot than for others in the set, which should have a small effect on the relaxed Hugoniot but might also promote unrelaxed behavior in this shot. However, the additional experiments 629 (Cu flyer at 1.55 km s^{-1}) and 655 (W flyer at 2.46 km s^{-1}), performed by Rigden and co-workers but not previously published, plot very close to the linear Hugoniot of *Rigden et al.* [1989] and provide significant extra confidence in fitting the low-pressure segment of this line. In any case, all the experiments have been included in subsequent analysis. Of the two new preheated light gas gun experiments on this composition, shot 378 yielded sharp, well-defined driver and sample cut-offs and very high precision data, whereas shot 363 has a complex sample arrival with a wide and asymmetrical dispersion in apparent arrival times, leading to much poorer precision.

[35] Unweighted linear regression of these data in U_s-u_p space yields C_o = 3420 ± 139 m s^{-1}, s = 1.43 ± 0.06, and r^2 = 0.989. This is within error of the original linear fit of *Rigden et al.* [1989]: C_o = 3300 m s^{-1}, s = 1.44. However, this fit is unsatisfactory at both ambient pressure and at the highest measured pressure. It fails by a large margin to recover the ambient pressure, 1773 K sound speed of the liquid, 3035 ± 21 m s^{-1} [*Ai and Lange*, 2008]. It also misfits the very high precision data point at u_p = 4403 m s^{-1} from shot 378 by 10 standard deviations. On the other hand, unweighted linear regression with the intercept pinned at the ultrasonic value yields a satisfactory fit to all constraints (except the re-analyzed shot 630), with C_o fixed at 3035 m s^{-1}, s = 1.57 ± 0.04, r^2 = 0.995. As we will discuss below, this higher value of s is also more consistent with the value of K'_S (7.0, similar to the values of 6.9 and 6.8 derived by *Rigden et al.* [1989] and *Ai and Lange* [2008], respectively) that emerges from fitting to a Birch-Murnaghan/Mie-Grüneisen EOS.

3.3. Anorthite

[36] The data for An liquid is shown in Figure 4. The re-analysis reproduces the six experiments in *Rigden et al.* [1989] within one overlapping standard deviation with the exception of shot 664, which requires 1.5 mutual standard deviations to overlap the original analysis. These revisions are not large enough to significantly change the fits to or conclusions from the low-pressure data given by *Rigden et al.* [1989]. None of the four new preheated light gas gun experiments on An yielded streak images with entirely satisfactory, simple sample cutoffs (e.g., Figure 1c), resulting in substantial uncertainty. It is possible that there exists a systematic reason for unsteady shock propagation in this material related to the complexity of its compression behavior.

[37] Simple regression of this data set is unsatisfactory. *Rigden et al.* [1989] noted that their six data points were difficult to fit with a single line and offered two regressions, one of which excluded their highest pressure datum. These two fits were given by C_o = 2680 m s^{-1}, s = 1.42 (excluding shot 672) and C_o = 2850 m s^{-1}, s = 1.27 (with all data). Neither of these fits comes close to predicting any of the new high-pressure data. A simple unweighted linear regression to the entire data set yields C_o = 2354 ± 114 m s^{-1}, s = 1.612 ± 0.04, r^2 = 0.996. Despite the high correlation coefficient, this line misfits shot 672 quite badly, has too high a slope in the region of the new high-pressure data, and most importantly is highly discrepant with the ambient pressure, 1923 K sound speed in this liquid, 2780 ± 23 m s^{-1} [*Ai and Lange*, 2008]. In this case, fixing the intercept to the ultrasonic value does not yield a good fit either, giving a line that passes systematically above all the low-pressure data and below all the high-pressure data. A quadratic fit ($U_s = C_o + su_p + qu_p^2$) does not seem warranted, since it gives an even higher slope in the region of the high-pressure data.

[38] The results of these exercises suggest that, contrary to the Di and $Di_{64}An_{36}$ compositions, An liquid displays some complexity in its shock compression behavior and cannot be described across the entire pressure range from 0 to 125 GPa by any straight line Hugoniot, particularly if the Hugoniot is considered to sample relaxed behavior and hence to originate at the ultrasonic sound speed point. The character of the anomaly that we see in An is different from the anomaly inferred for $Di_{64}An_{36}$ by *Rigden et al.* [1988]; in An the low-pressure and high-pressure segments appear to define nearly parallel lines with different intercepts, whereas the previously reported anomaly in the Hugoniot of $Di_{64}An_{36}$ was a sharp change in the slope. Thus the high-pressure segment of the An Hugoniot remains compressible, whereas the high-pressure segment of the *Rigden et al.* [1988] $Di_{64}An_{36}$ Hugoniot was nearly incompressible. We will revisit this issue and examine hypotheses for the origin of the complexity of the An Hugoniot below.

3.4. Solid Diopside-Anorthite Aggregate

[39] Shot 368 was carried out on solid $Di_{64}An_{36}$ polycrystalline aggregate initially at 300 K. This measured shock velocity is 870 ± 100 m s^{-1} faster than the linear fit to the

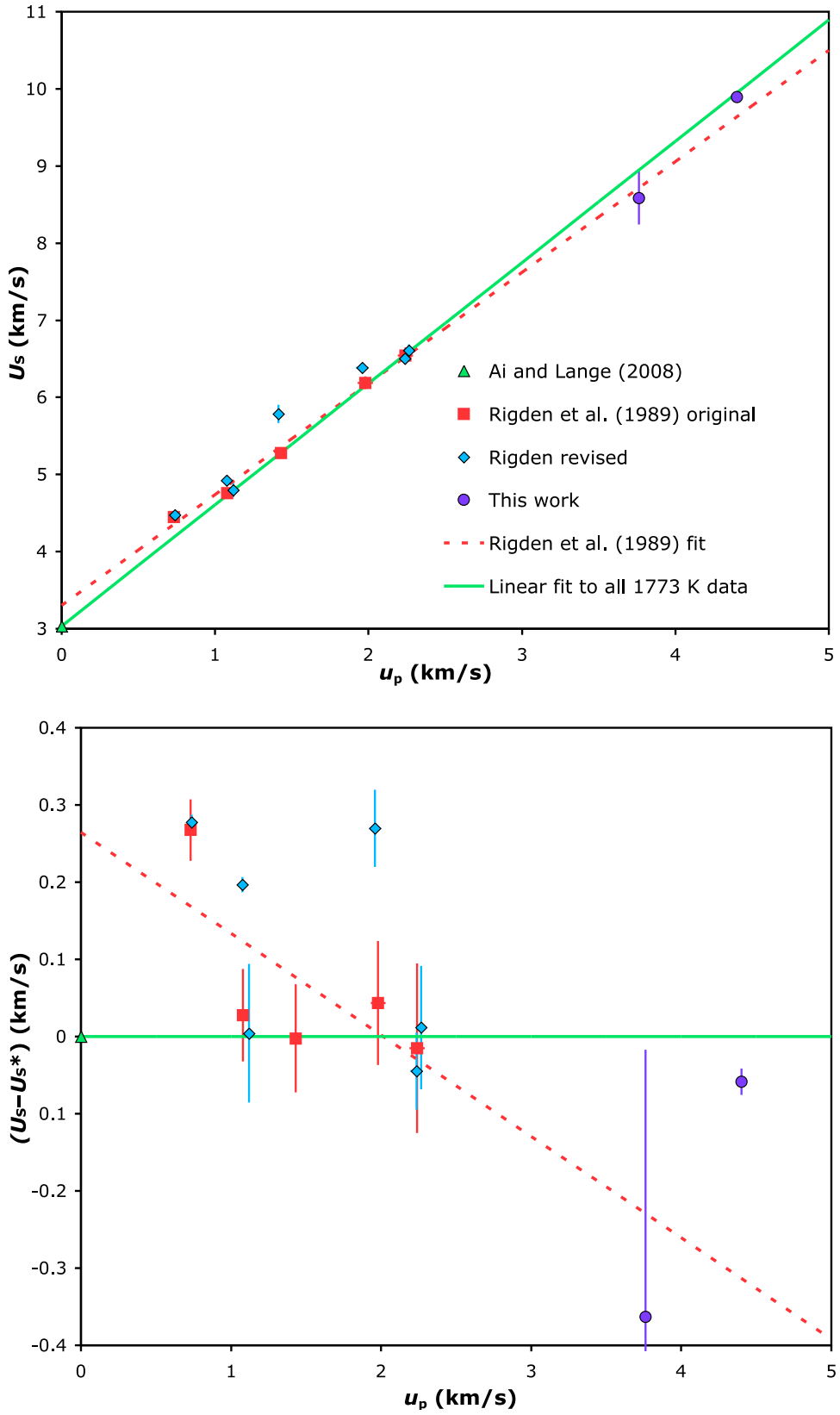

Figure 3. Hugoniot data for Di liquid preheated to ~1773 K. (a) U_s vs. u_p. (b) $U_s - U_s^*$ vs. u_p, where best fitting line is $U_s^* = 3035 + 1.571\ u_p$ m s^{-1}. Symbols as in Figure 2.

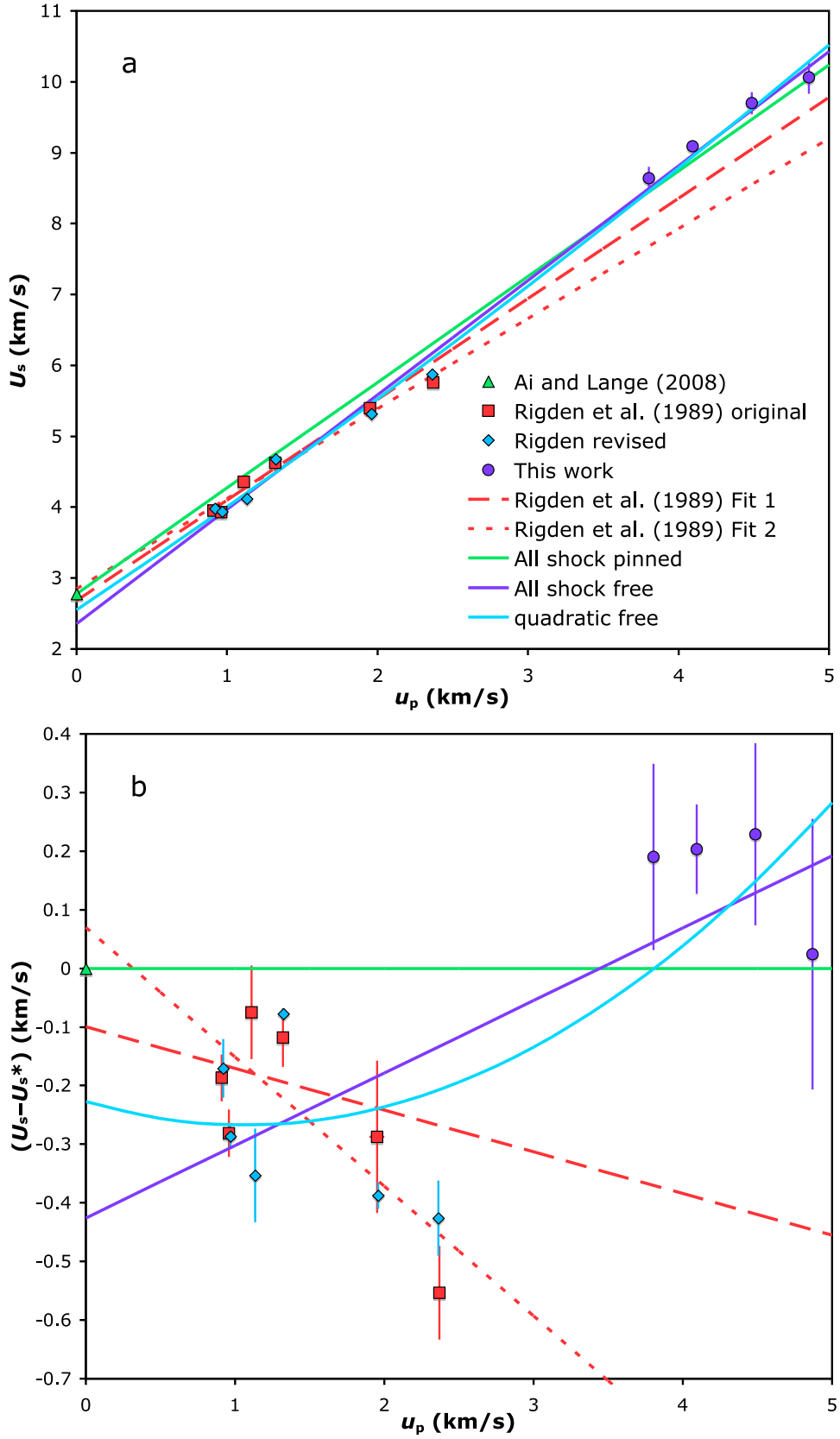

Figure 4. Hugoniot data for An liquid preheated to ~1923 K. (a) U_s vs. u_p. (b) $U_s - U_s^*$ vs. u_p, where the linear fit to all data, with intercept pinned at the ultrasonic sound speed, is $U_s^* = 2780 + 1.491\ u_p$ m s^{-1}. Data symbols as in Figure 2.

Hugoniot of the isochemical liquid from 1673 K at the same particle velocity (Figure 2), due to differences in the density (ρ) and internal energy (E) of the starting state. If the shock state at 133 GPa achieved in Shot 368 is molten, then the offset between these two Hugoniots can be used to define the Grüneisen parameter γ for this liquid, at the density sampled by this experiment. Although neither the liquidus nor the Hugoniot temperature of this composition is known well enough to define the limit for shock melting, we argue that this experiment is quite likely to have achieved a molten state. First, the pressure limit for complete shock melting has been determined for a number of related silicate minerals: quartz at 120 GPa [*Akins and Ahrens*, 2002; *Lyzenga et al.*, 1983], forsterite at 142 GPa [*Mosenfelder et al.*, 2007], diopside at ≤144 GPa [*Svendsen and Ahrens*, 1990], and enstatite at 174 GPa [*Mosenfelder et al.*, 2009]. The $Di_{64}An_{36}$ composition has an ambient pressure melting point at least 100 K lower than any of these and is expected therefore to have the lowest pressure of shock melting. Second, the Hugoniots of solid diopside to 179 GPa [single crystal data of *Svendsen and Ahrens*, 1983] and solid anorthite to 100 GPa [polycrystalline anorthosite data of *Mcqueen et al.*, 1967] each define linear high-pressure phase regimes. The Hugoniot of mixtures by kinetic-energy averaging theory of *Batsanov* [1994] has been found to be accurate to <1% (even for such disparate materials as tungsten and paraffin [*Petel and Jette*, 2010]); this model predicts the particle velocity of solid $Di_{64}An_{36}$ at P = 133.45 GPa to be u_p = 4.322 km s^{-1}, whereas the observed result in Shot 368 is u_p = 4.211 ± 0.016 km s^{-1}. The difference of over six standard deviations is highly significant and tends to exclude the hypothesis that the shock state in 368 is a solid aggregate of anorthite and diopside. We will fit this result in two ways, first as an offset to the linear Hugoniot in U_s-u_p space, and later as part of the overall fit to a thermal EOS in the next section.

[40] To obtain γ from U_s-u_p analysis, we proceed as follows. The definition of γ is

$$\gamma = \frac{1}{\rho}\left(\frac{\partial P}{\partial E}\right)_{\rho}. \tag{1}$$

The Mie-Grüneisen approximation is to take γ to be a function of ρ only, in which case we approximate (1) by

$$\gamma = \frac{1}{\rho}\frac{\Delta P}{\Delta E}, \tag{2}$$

where ΔP and ΔE are the differences in pressure and internal energy between any two thermodynamic states at equal ρ. In our case, these two states are (1) the experimentally determined Hugoniot point obtained by shocking the room temperature solid aggregate and (2) the point on the linear Hugoniot fitted to the preheated $Di_{64}An_{36}$ liquid experiments that has the same density as state (1). The pressure and density of state (1) are given in Table 2, under shot 368: P_1 = 133.45 GPa, ρ = 5209.13 kg m^{-3}. State (2) can be found from the fitted values for the liquid Hugoniot (C_o = 2963 m s^{-1}, s = 1.534) and the second Rankine-Hugoniot equation; we obtain P_2 = 204.85 GPa. We obtain ΔE from a thermodynamic cycle:

$$\Delta E = \Delta E_{H1} - \Delta E_{H2} + \Delta E_{tr}, \tag{3}$$

where ΔE_{H1} = 8869 kJ kg^{-1} is the internal energy jump across the shock in experiment 368, from the solid assemblage at 300 K to state (1), given by the third Rankine-Hugoniot equation; ΔE_{H2} = 19489 kJ kg^{-1} is the corresponding internal energy jump for the shock from the high-temperature liquid initial state to state (2); and ΔE_{tr} is the difference in internal energy between the two initial states. ΔE_{tr} is estimated from the enthalpy difference ΔH_{tr}, since this transition takes place essentially at zero pressure. ΔH_{tr} has two components: the isobaric heat capacity due to the temperature difference between 300 and 1673 K and the enthalpy of fusion. Both are obtained from the MELTS model [*Ghiorso and Sack*, 1995], which includes standard state data for diopside and anorthite solids and liquids and a mixing model that accounts for non-ideal mixing in the binary liquid. The value obtained is ΔE_{tr} = −1954 kJ kg^{-1}.

[41] Combining all these data gives γ = 1.09 for $Di_{64}An_{36}$ liquid at density 5209 kg m^{-3}. On the other hand, the Grüneisen parameter at the reference density ρ_o = 2618 kg m^{-3} can be obtained from the identities $\gamma = \alpha K_T/\rho C_V$ and $C_p/C_v = 1 + \alpha\gamma T$ and the following data: coefficient of thermal expansion α = 6.084 × 10^{-5} K^{-1} [*Lange*, 1997], formula weight = 238.749, isothermal bulk modulus K_{oT} = 22.3 GPa [*Ai and Lange*, 2008], and molar isobaric heat capacity C_p = 376.596 J K^{-1} mol^{-1} [*Ghiorso and Sack*, 1995]. The result is γ_o = 0.355. We find that, as previously reported experimentally and theoretically for forsterite [*Adjaoud et al.*, 2008; *Brown et al.*, 1987; *de Koker et al.*, 2008; *Mosenfelder et al.*, 2007] and enstatite [*Mosenfelder et al.*, 2009; *Stixrude and Karki*, 2005] compositions, the thermodynamic Grüneisen parameter of this liquid increases upon compression. Specifically, in all three compositions, γ increases by about a factor of three as ρ increases by a factor of about two. Fitting the one high-pressure constraint on γ derived from this experiment to a convenient functional form for the volume dependence of γ:

$$\gamma = \gamma_o\left(\frac{\rho_o}{\rho}\right)^q, \tag{4}$$

yields q = −1.63, which is remarkably similar to the q values reported for forsterite and enstatite liquids [*Mosenfelder et al.*, 2007; *Mosenfelder et al.*, 2009], suggesting that $-2.0 \le q \le -1.5$ may be a general behavior, at least for Fe-free mafic to ultramafic silicate liquids between $1 \ge \rho_o/\rho \ge 0.5$.

4. Thermal Equation of State Fitting

4.1. Theory

[42] A Hugoniot is only a partial description of the EOS of a phase, since it is a one-parameter function, *i.e.*, a curve through $\rho(P, T)$ or any other two-parameter space. Many of the thermodynamic states of interest for scientific and engineering applications are off the Hugoniot, often at lower temperature for a given pressure or volume. Here we use the term thermal EOS for a description of a phase that defines an entire surface such as $\rho(P, T)$ or $P(\rho, E)$. There are numerous functional forms that have been proposed for such a thermal EOS; its form is not known from rigorous theory. Here we test three formalisms. (1) The shock wave equation of state (SWEOS) is parameterized to 3rd order in strain by density at ambient pressure, a linear Hugoniot, and a

Table 3. Shock Wave Equation of State Fits

	Units	$Di_{64}An_{36}$	Diopside	Source[a]
T_o	K	1680.15	1781.15	
ρ_o	kg m^{-3}	2618	2619	L97
C_o	m s^{-1}	2963 ± 20	3035 ± 21	AL08
s		1.534 ± 0.016	1.571 ± 0.038	fitted
γ_o		0.356	0.493	AL08
q		−1.63		fitted
K_{So}	GPa	22.98	24.13	derived
K'		5.14	5.29	derived

[a]Sources: L97 is [*Lange*, 1997]. AL08 is [*Ai and Lange*, 2008]. Fitted indicates adjustable parameters. Derived indicated parameters calculated from other parameters given in the table. Note, fitting of SWEOS to anorthite data set yielded no acceptable overall fit. A constraint for q was only obtained for $Di_{64}An_{36}$.

Mie-Grüneisen thermal pressure. For $Di_{64}An_{36}$ we already presented such a fit above; for Di and An we lack sufficient data, since all our experiments lie very close to a single Hugoniot (differences of a few degrees in initial temperature are not enough to constrain q). Fits to the SWEOS are summarized in Table 3. (2) A 3rd or 4th order Birch-Murnaghan isentrope centered at 1 bar pressure and 1673 K, with a Mie-Grüneisen thermal pressure term, is labeled Birch-Murnaghan/Mie-Grüneisen (BM3/MG or BM4/MG). Fits to this EOS form are discussed below and given in Table 4. (3) Fits to the thermal EOS for silicate liquids introduced by *Ghiorso* [2004b] are given in Table 5. Since we are fitting Hugoniot data, the natural space in which to express our equations is $P(\rho, E)$; in order to apply formalisms or compare to data where temperature is a variable (measured or independent), it is necessary to add a definition of the heat capacity of the phase.

[43] The BM/MG EOS is defined by the following set of equations. The Eulerian finite strain parameter f is

$$f = \frac{1}{2}\left(\left(\frac{\rho}{\rho_o}\right)^{2/3} - 1\right). \tag{5}$$

The isentropic pressure P_s at strain f is given to 4th order by

$$P_S = 3K_{oS}f(1+2f)^{5/2}\left(1 + \frac{3}{2}\left(K_S' - 4\right)f + \frac{3}{2}\left(K_S'' K_{oS} + K_S'\left(K_S' - 7\right) + \frac{143}{9}\right)f^2\right), \tag{6}$$

where K_{oS} is the isentropic bulk modulus at zero pressure, K'_S is the isentropic first derivative of K_S with respect to pressure at zero pressure, and K''_S is the isentropic second derivative of K_S with respect to pressure at zero pressure. This can be reduced to 3rd order by either dropping the quadratic term in the power series in f or by choosing K''_S such that this term vanishes. The internal energy change along the isentrope is given by integration of $dE_S = -P_S dV$:

$$E_S = \frac{9}{2}\frac{K_{oS}}{\rho_o}\left(f^2 + \left(K_S' - 4\right)f^3 + \frac{3}{4}\left(K_S'' K_{oS} + K_S'\left(K_S' - 7\right) + \frac{143}{9}\right)f^4\right). \tag{7}$$

The total pressure at any volume and internal energy is found as an offset from the isentrope in the Mie-Grüneisen approximation:

$$P = P_S + \gamma\rho(E - E_S). \tag{8}$$

The temperature is given by integrating along the isentrope to the density of interest and then adding an energy offset proportional to C_V:

$$T = T_o \exp\left[\int_{\rho_o}^{\rho} \frac{\gamma}{\rho} d\rho\right] + \int_{E_S}^{E} \frac{1}{C_V} dE, \tag{9}$$

where T_o = 1673 K is the foot temperature of the reference isentrope.

[44] The full set of parameters defining the thermal EOS of a liquid in this model is then: ρ_o, K_{oS}, K'_S, γ_o, q, and C_V; plus K''_S if a 4th-order treatment is necessary. In most of the fitting in this work, we take ρ_o, K_{oS}, γ_o, and C_V as fixed

Table 4. Birch-Murnaghan/Mie-Grüneisen Equation of State Fits

	Units	Anorthite compound BM3	BM4*	$Di_{64}An_{36}$ BM3	$Di_{64}An_{36}$ BM4	Diopside BM3	Diopside BM4	Source[a]
ρ_o	kg m^{-3}	2585	2585	2618	2618	2643	2643	L97
K_{So}	GPa	20.39	20.39	22.98	22.98	24.57	24.57	AL08
K'_S		6.00	1.76	5.36	4.66	6.98	9.44	fitted
K''_S	GPa^{-1}		+0.726		−0.149		−2.55	fitted
γ_o		0.173	0.180	0.356	0.356	0.493	0.493	AL08
q		0.756	−1.71	−2.059	−1.784	−0.597	−2.571	fitted
C_V	J K^{-1} kg^{-1}	1512.9	1512.9	1519.5	1519.5	1506.2	1506.2	LN92
ρ_o^{HPP}	kg m^{-3}	4225						fitted
K_{So}^{HPP}	GPa	256.6						fitted
K''^{HPP}_S		3.23						fitted
γ_o^{HPP}		2.632						fitted
q^{HPP}		3.787						fitted
V_{crit}	m^3 kg^{-1}	2.393 × 10^{-4}						fitted
V_{width}	m^3 kg^{-1}	9.473 × 10^{-6}						fitted

[a]Sources: L97 is [*Lange*, 1997]. AL08 is [*Ai and Lange*, 2008]. Fitted indicates adjustable parameters. All fits anchored at T_o = 1673.15 K. BM3 = 3rd order Birch-Murnaghan isentrope. BM4 = 4th order Birch-Murnaghan isentrope. See text for explanation of compound BM3 fit. * = fit excluding Anorthite shots 663 and 672 of *Rigden et al.* [1989].

Table 5. Ghiorso Equation of State Fits

	Units	Anorthite	$Di_{64}An_{36}$	Diopside	Source[a]
V	$cm^3\ mol^{-1}$	107.67	91.2	81.94	L97
$(\partial V/\partial T)_P$	$cm^3\ mol^{-1}\ K^{-1}$	3.740×10^{-3}	5.832×10^{-3}	7.010×10^{-3}	L97
α	K^{-1}	3.474×10^{-5}	6.396×10^{-5}	8.555×10^{-5}	derived
c	$m\ s^{-1}$	2811.75	2963.75	3049.25	AL08
$(\partial c/\partial T)_P$	$m\ s^{-1}\ K^{-1}$	−0.1275	−0.1275	−0.1275	AL08
MW	$g\ mol^{-1}$	278.21	238.76	216.56	
C_P	$J\ mol^{-1}\ K^{-1}$	425.3	376.6	349.2	LN92
$(\partial V/\partial P)_T$	$cm^3\ mol^{-1}\ GPa^{-1}$	−5.32527	−4.11724	−3.56992	derived
$(\partial^2 V/\partial P^2)_T$	$cm^3\ mol^{-1}\ GPa^{-2}$	1.15553	2.87403	0.738669	fitted
$(\partial^3 V/\partial P^3)_T$	$cm^3\ mol^{-1}\ GPa^{-3}$	−0.356501	−7.01648	−0.229262	fitted
$(\partial^4 V/\partial P^4)_T$	$cm^3\ mol^{-1}\ GPa^{-4}$	0.132672	25.39584	−0.034277	fitted
a	GPa^{-1}	0.281085	0.973266	137499.6	derived
b	GPa^{-2}	0.019339	0.055665	14225.3	derived
ρ	$kg\ m^{-3}$	2583.9	2618.0	2642.9	derived
K_s	GPa	20.43	23.00	24.57	derived
γ_o		0.18	0.36	0.49	derived

[a]Sources: L97 is [*Lange*, 1997]. AL08 is [*Ai and Lange*, 2008]. LN92 is [*Lange and Navrotsky*, 1992]. Fitted indicates adjustable parameters. Derived indicated parameters calculated from other parameters given in the table (see [*Ghiorso*, 2004b]).

parameters based on data from ambient pressure experimental methods [*Ai and Lange*, 2008; *Lange and Navrotsky*, 1992; *Lange*, 1997] and we adjust only K'_S, q, and sometimes K''_S; the exception is a more complicated fit for Anorthite liquid, explained below. Use of a constant C_V is a limitation of the theory, but we lack any shock temperature measurements or other data on liquids of similar composition that might constrain the volume dependence of C_V.

[45] In order to fit shock wave data to this EOS, we account for uncertainty in both the experimental pressure P_H and density ρ_H. This is accomplished by minimizing a total χ^2 function

$$\chi^2 = \sum_{i=1}^{n} \left[\left(\frac{P_*^i\left(\rho_*^i\right) - P_H^i}{\sigma_P^i} \right)^2 + \left(\frac{\rho_*^i - \rho_H^i}{\sigma_\rho^i} \right)^2 \right], \qquad (10)$$

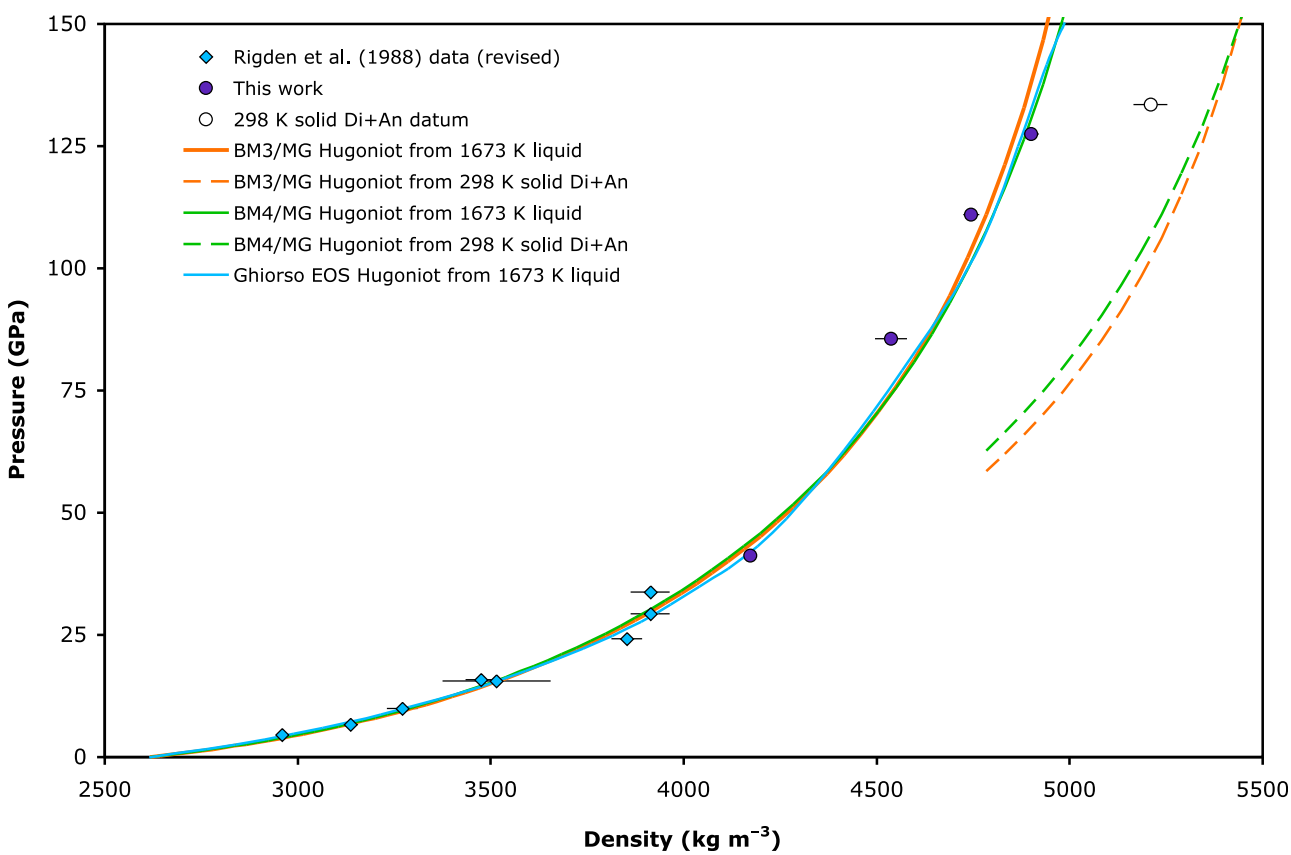

Figure 5. Hugoniot data and thermal EOS fits for $Di_{64}An_{36}$ liquid and polycrystalline solid, plotted in pressure (P) vs. density (ρ). Data symbols as in Figure 2.

where in a set of n experiments, each experimental pair (P^i_H, ρ^i_H) has uncertainties (σ^i_P, σ^i_ρ) and the minimization of this function involves searching over the unknown parameters in the EOS as well as over the n trial values of density ρ^i_*, where the trial pressure P^i_* is evaluated along the model Hugoniot at the trial density. The calculation of P^i_* is given by [for a derivation see the appendix to *Akins et al.*, 2004]:

$$P^i_* = \frac{P_S - \gamma\rho^i_*\left(E_S + E^i_{tr}\right)}{1 - \frac{\gamma}{2}\left(\frac{\rho^i_*}{\rho^i_o} - 1\right)}, \tag{11}$$

where P_S, E_S and γ are all evaluated at the trial density ρ^i_* (using equations (6), (7), and (4), respectively), and each experiment has its own value of E^i_{tr} and ρ^i_o because both these parameters depend on the initial temperature, which varies by a few degrees within each data set. We obtain ρ^i_o from the partial molar volumes and thermal expansion coefficients given by *Lange* [1997]. Transition energy in this case is due to the offset in initial temperature of the experiment from the reference temperature of 1673 K, and is obtained using the temperature-independent values of partial molar isobaric heat capacity from *Lange and Navrotsky* [1992]. The goodness of fit is evaluated using a reduced χ^2 parameter, $\chi^2/(n - m)$, where m is the number of free model parameters in the fit (not including the trial density values). Error bounds on the fitted parameters and the degree of correlation among those parameters are estimated by bootstrap analysis [*Efron*, 1982].

[46] The Ghiorso EOS (GEOS) is defined by *Ghiorso* [2004b] and the method of fitting it to shock wave data is explained in *Ghiorso* [2004a]. The equation has 8 parameters, all defined at a reference temperature and pressure of 1673 K and 1 bar: the molar volume (V) and $(\partial V/\partial T)_P$; the sound speed ($c$) and $(\partial c/\partial T)_P$; the isobaric heat capacity (C_P); and the pressure derivatives $(\partial^2 V/dP^2)_T$, $(\partial^3 V/dP^3)_T$ and $(\partial^4 V/dP^4)_T$. For the present application, the first five of these are taken as fixed (data sources in Table 5). The free parameters are the derivatives in the Taylor series for volume vs. pressure, expanded about 1673 K and 1 bar: $(\partial^2 V/dP^2)_T$, $(\partial^3 V/dP^3)_T$ and $(\partial^4 V/dP^4)_T$. The fitting algorithm is similar to the one described above and considers errors in both pressure and density. *Ghiorso* [2004b] gives formulas for a number of derived parameters within this EOS formalism, including γ, which will prove useful for comparing predictions of the various equations of state being tested.

4.2. $Di_{64}An_{36}$

[47] The BM/MG fit for the eutectic composition is based on data in Table 2. The BM3/MG fit, keeping all the ambient pressure parameters fixed, yields $K'_S = 5.35 \pm 0.43$, $q = -2.20 \pm 0.54$, with a reduced χ^2 value of 4.5 (Figure 5). The uncertainties on K'_S and q are correlated (correlation coefficient = +0.54), implying that their individual errors overstate the uncertainty of the fit. We also examined a 4th-order Birch-Murnaghan isentrope, adding K'_S as a free parameter; the result is a slightly better fit, with reduced χ^2 value of 3.9. In this fit, $q = -1.99$ is within error of the 3rd-order best-fit value, whereas $K'_S = 4.63$ and $K'_S = -3.61 \times 10^{-11}$ GPa^{-1}. For this composition we recommend the 3rd-order fit. When fitting these formalisms, the data along the preheated liquid Hugoniot place significant constraints on q, so unlike the SWEOS fit above we cannot simply vary q to exactly fit the room-temperature solid datum. In fact, given the fairly large error bars on shot 368 (due in part to the use of a very thin sample), it has a minor influence on the present fitting exercise, and the values of q are somewhat different from the result of −1.63 given above. Nevertheless, $q \sim -2$ is in the neighborhood of values observed for other silicate liquids under shock compression and $K'_S = 5.35$ is, within error, identical to the value of 5.6 derived by *Ai and Lange* [2008] from ultrasonic and low-pressure shock wave data.

[48] Figure 5 also shows the GEOS fit to the $Di_{64}An_{36}$ Hugoniot. We see that it is essentially indistinguishable in this case from the 3rd or 4th-order Birch-Murnaghan fits, as viewed along the Hugoniot and in its ability to fit the data. However, as we discuss below, it makes very different predictions for thermodynamic conditions far from the Hugoniot. In particular, the behavior of γ at high compressions is unsatisfactory in this particular instance of the GEOS (see section 5 below).

4.3. Diopside

[49] The data set for diopside, lacking an off-Hugoniot point and containing one outlier and one low-precision high-pressure point, is more difficult to fit than the eutectic composition. Trade-offs between K'_S and q are particularly severe. The best-fitting 3rd order BM/MG model has $K'_S = 6.98$, $q = -0.60$, and reduced $\chi^2 = 4.26$. This fit lies near the middle of a narrow "valley" of almost equally good solutions extending from $K'_S \sim 6$, $q \sim -1.4$ towards $K'_S \sim 8$, $q \sim +2.3$. With little basis to choose among these models, we adopt the choice of best fitting value for K'_s, since it lies very close to the recommended value of 6.8 from *Ai and Lange* [2008] (Figure 6). We also carried out a 4th-order BM/MG fit for this composition; the result is $K'_S = 9.44$, $K'_S = -2.55 \times 10^{-9}$ GPa^{-1}, $q = -2.57$, reduced $\chi^2 = 2.79$. This appears to be a significantly better fit, but it may be over-fitting the available data. Moreover, the very large value of K'_S makes this fit hard to compare to 3rd-order fits by other groups and causes a singularity on the extrapolated EOS at $\rho = 4850$ kg m^{-3}, just slightly beyond the measured pressure range. Again we recommend the 3rd-order fit for this composition. Figure 6 also shows the GEOS fit to the diopside data, which is rather poor; it fits the new highest-pressure datum well but systematically overestimates volume for all the *Rigden et al.* [1989] data.

[50] We examined the shock temperature data collected on diopside single crystals near 150 GPa and $CaMgSi_2O_6$ glass near 90 GPa by *Svendsen and Ahrens* [1990] to test whether these results could be used to constrain the thermal EOS of diopside melt off the preheated liquid Hugoniot. However, the assignment of these shock states to melt is unclear and also the measurement of travel time from the radiance records proved too imprecise to be useful. Hence we have not included these data in our fitting.

4.4. Anorthite

[51] In our view, the overall anorthite data set cannot be well fit by a single straight line Hugoniot in U_s-u_p space. In the case of 3rd order BM/MG fitting, we obtain a fairly well defined solution at $K'_S = 3.94 \pm 0.18$, $q = -3.48 \pm 0.14$,

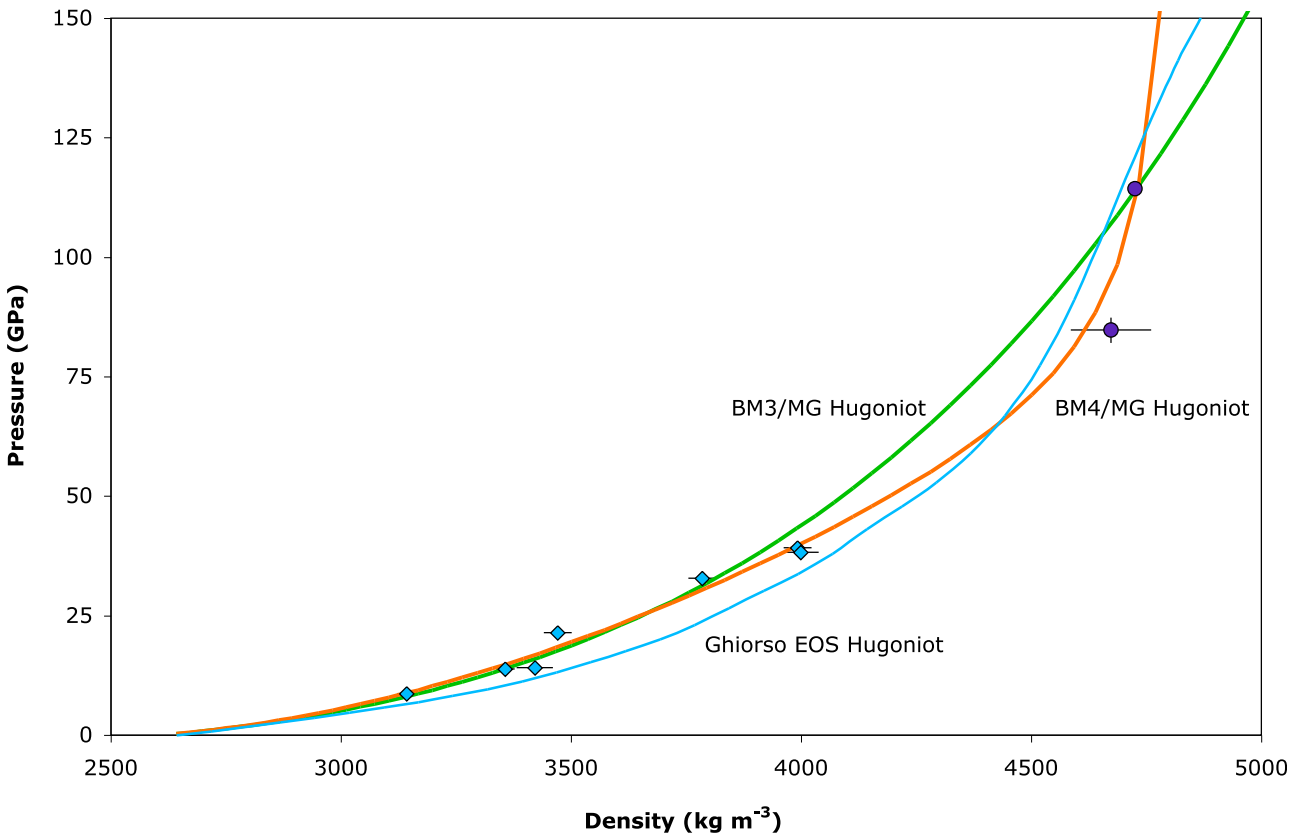

Figure 6. Hugoniot data and thermal EOS fits for Di liquid, plotted in pressure (P) vs. density (ρ). Data symbols as in Figure 2.

reduced $\chi^2 = 0.285$. Despite its small reduced χ^2, this fit is also unsatisfactory (Figure 7) because it clearly has the wrong slope through the four high-pressure data points and a very unlikely $K'_S/(4s - 1) = 0.8$ (using the value of s for a straight line fit to all the shock data constrained to C_o from the ultrasonic data). There is little room to seek a better set of fitted parameters within the family of solutions in this case, since the parameter trade-offs are rather limited. Instead we will consider models that do not attempt to fit the whole data set with a single set of parameters. There are two strategies: a compound fit to the whole data set and a fourth-order fit that excludes the two points suspected of being unrelaxed. We examine these two approaches in turn.

[52] It seems perhaps rather arbitrary to introduce a compound EOS for anorthite when four other compositions have been successfully described by single fits. That is, above we found 3rd order fits that extend from ambient pressure to 125 GPa for $Di_{64}An_{36}$ and diopside, whereas *Mosenfelder et al.* [2009] defined 4th order fits that extend from ambient pressure to 250 GPa for $MgSiO_3$ and to 200 GPa for Mg_2SiO_4. However, there are prior reasons to expect complexity in the anorthite system. First, the *Rigden et al.* [1989] data set on this composition was already difficult to fit to a straight-line Hugoniot; although the anomaly seen by *Rigden et al.* [1988] in $Di_{64}An_{36}$ is not confirmed by our data, perhaps the anorthite anomaly is hinting at real complexity. Moreover, this composition has been studied in detail by molecular dynamics (MD) simulations by *Spera et al.* [2009] and *Ghiorso et al.* [2009] and the behavior seen in their simulations closely resembles in some respects the complexity seen in our experiments. Specifically, they find rapid coordination changes upon compression around Si, Al, Ca, and O that are largely accomplished by 20 GPa and they need to use two different fitting regions at low and high pressure (with a boundary near 20 GPa) in order to successfully fit the MD densities. Furthermore, their fitted EOS displays a region of polyamorphism or liquid immiscibility in this one-component system. It is not clear at this time why anorthite should display complex compression behavior when the other liquids we have studied do not. All silicate liquids that have been studied spectroscopically or by MD show increases in cation coordination and network topology rearrangements with pressure, with most rapid changes in the 0–5 GPa range; anorthite is not especially unique in this regard. One possibility suggested by the results of *Spera et al.* [2009] concerns the O sublattice, which shows an increase in mean O–O 2nd nearest neighbor coordination number from 7 to 10, distributed over a range of 0–20 GPa. Anorthite is the most polymerized network liquid in our study, and it is possible that the oxygen sublattice compression behavior only displays a strong deviation from simple EOS behavior for highly polymerized liquids. In any case, the success of a compound EOS fit to the MD results is sufficient to motivate an attempt to fit a compound EOS to the shock wave data.

[53] In contrast to the approach of *Ghiorso et al.* [2009] with a sharp boundary between the fitting regions, we adopted a model that allows a gradual transition. At each

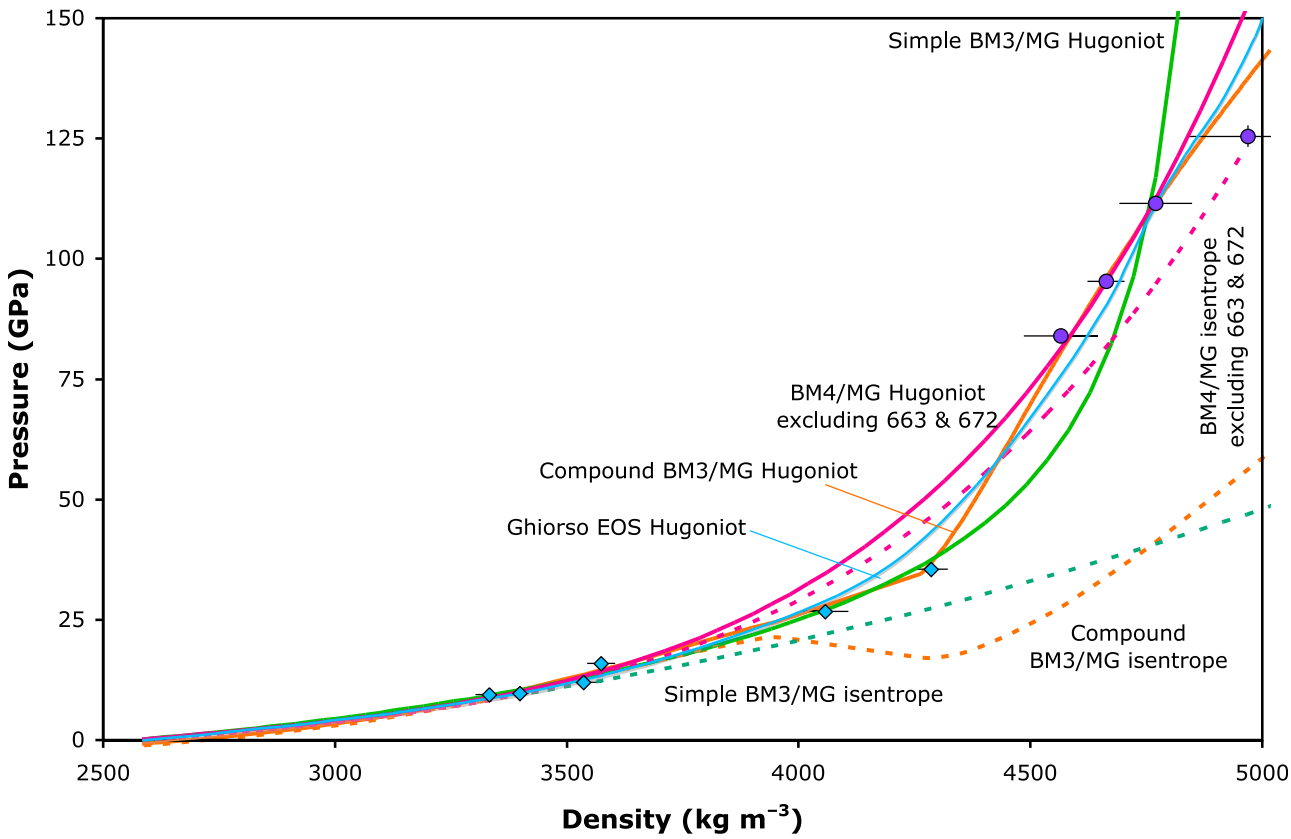

Figure 7. Hugoniot data and thermal EOS fits for An liquid, plotted in pressure (P) vs. density (ρ). Data symbols as in Figure 2. See text for discussion of the different strategies adopted for fitting this composition.

density, we replace the isentropic pressure from equation (6) with the sum of two components

$$P_S = x^{LPP} P_S^{LPP} + \left(1 - x^{LPP}\right) P_S^{HPP}, \tag{12}$$

where $0 \le x^{\mathrm{LPP}} \le 1$ is the parameter describing the transition from low pressure phase (LPP) behavior to high pressure phase (HPP) behavior. $P_{\mathrm{S}}^{\mathrm{LPP}}$ and $P_{\mathrm{S}}^{\mathrm{HPP}}$ are each given by a 3rd order Birch-Murnaghan expression, evaluated at the common density ρ, but with independent parameters ρ_{o}, K_{oS}, K'_{S} and $\rho_{\mathrm{o}}^{\mathrm{HPP}}$, $K_{\mathrm{oS}}^{\mathrm{HPP}}$, $K_{\mathrm{S}}^{\mathrm{HPP}}$, respectively. The internal energy of isentropic compression is given by a similar expression, mixing two expressions like equation (7) in proportions given by x^{LPP}. We also treat γ as a mixture between the two components,

$$\gamma = x^{LPP}\gamma_o\left(\frac{\rho_o}{\rho}\right)^q + \left(1 - x^{LPP}\right)\gamma_o^{HPP}\left(\frac{\rho_o^{HPP}}{\rho}\right)^{q^{HPP}}. \tag{13}$$

Given these mixing rules for P_{s}, E_{s}, and γ, equation (11) is used to obtain the Hugoniot pressure P_{H} for comparison to data using the χ^2 parameter from equation (10). There are two additional free parameters that define the center and width of the transition region as a function of density:

$$x_{LPP} = \frac{1}{\pi}\arctan\left(\frac{1/\rho - V_{crit}}{V_{width}}\right) + 0.5. \tag{14}$$

The compound fit inevitably has a large number of parameters, since there are no ambient pressure data to constrain the high-pressure part of the EOS. We are fitting nine data points with nine free parameters: K'_{S}, $\rho_{\mathrm{o}}^{\mathrm{HPP}}$, $K_{\mathrm{oS}}^{\mathrm{HPP}}$, $K_{\mathrm{S}}^{\mathrm{HPP}}$, q, $\gamma_{\mathrm{o}}^{\mathrm{HPP}}$, q^{HPP}, V_{crit} and V_{width}. We continue to keep the values of ρ_{o}, K_{oS} and γ_{o} fixed from ambient pressure measurements.

[54] The results of the fit are shown in Figure 7 and the behavior of x^{LPP} and γ are shown in Figure 8. Not surprisingly, given the large number of parameters, this model fits the data well; the reduced χ^2 is similar to the simple BM3/MG fits to the other compositions, which justifies the number of parameters used. What is more remarkable is the parameters that emerge.

[55] First, the model adopts a rather sharp transition: $V_{\mathrm{width}} = 9.47 \times 10^{-6}$ m^3 kg^{-1} centered at a density $1/V_{\mathrm{crit}} = 4178$ kg m^{-3} (that is, at $\rho_{\mathrm{o}}/\rho = 0.619$ and at 28 GPa on the Hugoniot), which corresponds to ≥90% LPP component at densities below 3500 kg m^{-3} and ≤10% LPP at densities above 4988 kg m^{-3}. This is rather similar to the transition pressure and width adopted by *Ghiorso et al.* [2009] to fit the MD state data for anorthite.

[56] Second, the value of $K'_{\mathrm{S}} = 6$ is significantly larger than the value of $K'_{\mathrm{S}} = 4.7$ recommended by *Ai and Lange* [2008] based on ambient pressure sound speed and low-pressure Hugoniot data. This suggests that the low-pressure segment of our Hugoniot is already influenced by coordination change, and that the LPP properties of the compound

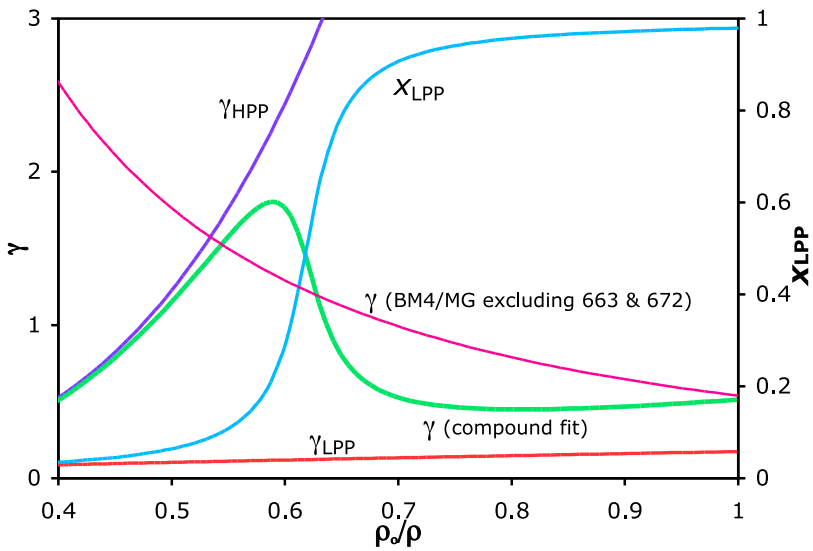

Figure 8. Behavior of the compound fit to the An EOS: On the right-hand scale, the fraction of low-pressure phase (LPP) component; and, on the left-hand scale: the Grüneisen parameter (γ^{LPP}) of the LPP component, the Grüneisen parameter of the high-pressure phase (γ^{HPP}) component, and the Grüneisen parameter of the compound fit (γ) as functions of density normalized to the 1 bar, 1673 K reference density of the LPP EOS (ρ_o/ρ). The fourth-order Birch-Murnaghan/Mie-Grüneisen fit to the anorthite data set excluding two experiments by *Rigden et al.* [1989] that are suspected of unrelaxed behavior is also shown.

fit are only a good description of this liquid in the limit of near-zero pressure. Coordination changes begin to have a noticeable effect on the compression behavior of this liquid at less than 10 GPa.

[57] Third, the ambient pressure density of the high-pressure segment, $\rho_o^{HPP} = 4225$ kg m^{-3}, is 7% larger than the density of an isochemical mixture of the dense oxides lime, corundum, and stishovite. *Rigden et al.* [1989] proposed that liquid silicate densities approach within 10% the densities of corresponding mixtures of dense oxide phases by about 40 GPa. This is taken as evidence that by this pressure coordination changes in the melt phase have largely transformed Si and Al ions into structural units similar to those in stishovite and corundum. The reference density of our HPP segment appears to be consistent with this hypothesis. Furthermore, the bulk modulus of the HPP component, $K_{oS}^{HPP} = 256.6$ GPa, while over 10 times larger than the bulk modulus of anorthite liquid at ambient pressure, is only 5% larger than the Voigt average estimate and 13.6% larger than the Voigt-Reuss-Hill average estimate of the bulk modulus of an aggregate of lime, corundum and stishovite. Together with the small $K_S'^{HPP} = 3.235$ estimate, these parameters suggest that the high-pressure behavior of anorthite liquid remains similar to the dense oxide mixture over a wide pressure range, perhaps crossing over to higher density at very high pressure.

[58] Fourth, both the LPP and HPP segments yield positive q-values, as might be expected for compression behavior without change in coordination, as in a solid phase of fixed symmetry. However, the average Grüneisen parameter of the two-component mixed EOS increases over a wide compression range $0.81 \geq \rho_o/\rho \geq 0.59$, as the mixing fraction of HPP gradually increases. It reaches a maximum value $\gamma = 1.8$, similar to the values obtained at $\rho_o/\rho \sim 0.5$ for other highly-coordinated silicate liquids. This result seems very consistent with the conceptual suggestion of *Stixrude and Karki* [2005] that increasing γ in silicate liquids is the result of changes to higher coordination with increasing pressure.

[59] Fifth, although this EOS is constrained only by data along the Hugoniot, Figure 7 also shows the isentrope (that is, the first term on the right-hand side of equation 8) derived for anorthite liquid. Evidently, the isentrope predicted by extrapolation of this rather poorly constrained fit is highly uncertain, but we show it because it has interesting properties. Between densities of 4000 and 4300 kg m^{-3}, the isentrope has a negative slope, indicating an unstable region. This is consistent with the observation of a critical point and polyamorphism in the EOS of this material fit to MD constraints by *Ghiorso et al.* [2009], although that miscibility gap is at much lower pressure and higher volume than the one seen here.

[60] Figure 7 shows a fit of the *Ghiorso* [2004b] EOS to the anorthite liquid shock data set. This fit has a single set of parameters and is constrained by actual shock data; it should not be confused with the compound fit to molecular dynamics data introduced by *Ghiorso et al.* [2009]. Nevertheless, it yields an interesting compromise between the simple and compound Birch-Murnaghan fits. Like the fits to molecular dynamics data offered by *Ghiorso et al.* [2009] and also by *de Koker* [2010], the GEOS yields an acceptable fit to the data set except for the two highest-pressure data points from *Rigden et al.* [1989]. In particular, the GEOS yields a slope through the four highest-pressure data points close to that of our compound fit. As with the fits to the other compositions, although the Hugoniot fits look similar, computed off-Hugoniot states from these formalisms are quite different.

[61] The two highest-pressure Rigden data points, including shot 672 that *Rigden et al.* [1989] excluded from one version of their linear fit, are also those that *Ghiorso et al.* [2009] and *de Koker* [2010] attribute to possible unrelaxed (i.e., glass-like) behavior. There are two aspects of this attribution that deserve comment. First, it seems odd that the Hugoniot should sample relaxed behavior at low pressure and again at high pressure, with an unrelaxed region in between. We speculate that this results from the competition between two effects: (1) the continuous increase in shock temperature with increasing pressure along the Hugoniot, leading to lower viscosity and shorter relaxation times and (2) the increasing strain involved in transforming from zero pressure to higher-pressure states along the Hugoniot, leading to increasing strain rates within the shock front. This may produce an intermediate range along the Hugoniot where the strain rate is high enough and the relaxation time long enough to sample unrelaxed behavior. Second, it also seems odd that unrelaxed compression should yield densities *higher* than the relaxed Hugoniot at equal pressure. This is contrary to the usual behavior of relaxed and unrelaxed moduli, e.g. in ultrasonic experiments, where unrelaxed moduli are stiffer [e.g., *Rivers and Carmichael*, 1987] and so imply achievement of *lower* density for a given pressure. Again, we speculate that there are two effects at play: Hugoniot compression involves both pressure and temperature increase, and the relaxation mechanisms and times for these may be different. If response to increasing pressure occurs by local changes in bond lengths, angles, and coordination numbers [e.g., *Wolf and McMillan*, 1995], whereas response to increasing temperature involves also relatively long-range phenomena such as ring statistics and network topologies [e.g., *Dingwell*, 1995], we might then imagine achieving relaxed compression in response to applied pressure without achieving fully relaxed thermal expansion. The result would be higher density than a fully relaxed state at equal P and T.

[62] Given the possibility that points 663 and 672 are anomalous, we also investigate Birch-Murnaghan/Mie-Grüneisen fitting of the An data set excluding these two points. As suggested by the failure of the remaining data to follow a simple linear U_s-u_p Hugoniot with an intercept consistent with the ultrasonic data (Figure 4), we do not find an acceptable 3rd order fit. However, the 4th order fit is successful, which is consistent with the success of *de Koker* [2010] in fitting MD data to a 4th order expansion of the isentrope formalism of *de Koker and Stixrude* [2009] and recovering the shock data except for shots 663 and 672. The fit parameters (Table 4) are $K'_S = 1.76$, $K'_S = 7.26 \times 10^{-10}$ GPa^{-1}, $q = -1.71$, reduced $\chi^2 = 1.23$. Although this value of K′ seems highly anomalous and inconsistent with the slope of the U_s-u_p line, term-by-term comparison of 3rd and 4th-order fits is unwise. This fit is better evaluated by its ability to fit data than by the values of the individual fit parameters. One notable aspect of this fit is a much smaller thermal pressure term at high pressure than the compound fit, resulting in an isentrope much closer to the Hugoniot. In fact, the highest-pressure An shock datum plots within error on the model isentrope, despite the high temperature expected for this state. This appears consistent with the observation of *Ghiorso et al.* [2009] that the EOS fit to the MD data of *Spera et al.* [2009] predicts an isentrope (rather than a Hugoniot) that passes through these shock wave data (though that may also be due to shortcomings of the potential function adopted in that study).

5. Discussion

5.1. Comparison of Shock Wave to Ultrasonic Data for Molten Silicates

[63] The relationship between the shock wave EOS and finite strain theories such as the Birch-Murnaghan EOS is discussed in detail by *Jeanloz* [1989]. He shows that, despite the simple relationship $K'_S = 4s - 1$ that holds at zero strain, experimental values of K'_S from ultrasonic studies on pure elements are often ~20% larger than (4s-1) from Hugoniot measurements on the same materials [*Steinberg*, 1982]. The lower bound of $K'_S/(4s - 1)$ ratios is predicted fairly well by comparison of the linear SWEOS to the 3rd order Eulerian finite-strain (i.e., Birch-Murnaghan) EOS at $V/V_o = 0.5$, which further predicts that the ratio $K'_S/(4s - 1)$ should be 1.2 at $K'_S = 7$ [*Jeanloz*, 1989]. However, the actual elements often show $K'_S/(4s - 1)$ greater than this relationship by ~0.1. In this context, the diopside fits of *Rigden et al.* [1989], with $s = 1.33$ in the Hugoniot regression and $K'_S = 6.9$ in the Birch-Murnaghan fit, are highly anomalous with $K'_S/(4s - 1) = 1.45$. This suggests that extrapolation of the Hugoniot data alone down to zero strain yields an inconsistent result. On the other hand, our preferred linear Hugoniot for diopside liquid at 1773 K, with the sound speed at ambient pressure fixed to the ultrasonic value of *Ai and Lange* [2008], has $s = 1.57$. In combination with the value of $K'_S = 6.8$ from *Ai and Lange* [2008], which is also consistent with the current fitting exercise, we obtain $K'_S/(4s - 1) = 1.29$, which closely resembles the typical behavior of the elements, extrapolated to $K'_S = 6.8$. Although silicate liquids need not obey the systematics observed for solid elements, this result lends considerable confidence to the self-consistency of the EOS derived from the ultrasonic and shock wave data together.

5.2. Prediction of Off-Hugoniot States by Various Equations of State

[64] None of the thermal EOS formalisms we have applied has any strong theoretical claim to being a correct description of the thermodynamics of silicate liquids. Each involves a certain number of empirical assumptions, parameters held constant for convenience, or series truncated at an arbitrary number of terms. Yet each of them is able to fit data along the Hugoniot equally well, along with a certain amount of ancillary data at off-Hugoniot states. Specifically, all the models applied herein are constrained to fit thermal expansion, sound speed, and heat capacity data across a wide range of temperatures at 1 atmosphere. The SWEOS and Birch-Murnaghan-Mie-Grüneisen are formally identical expansions to 3rd order at zero strain. Furthermore, they use the same thermal pressure formulation, but nevertheless the fits are distinct at finite strain and can be expected to become increasingly different at larger strains, away from the common calibration points. The GEOS is already different from the others even at zero strain, and since its thermal pressure is formulated differently it can be expected

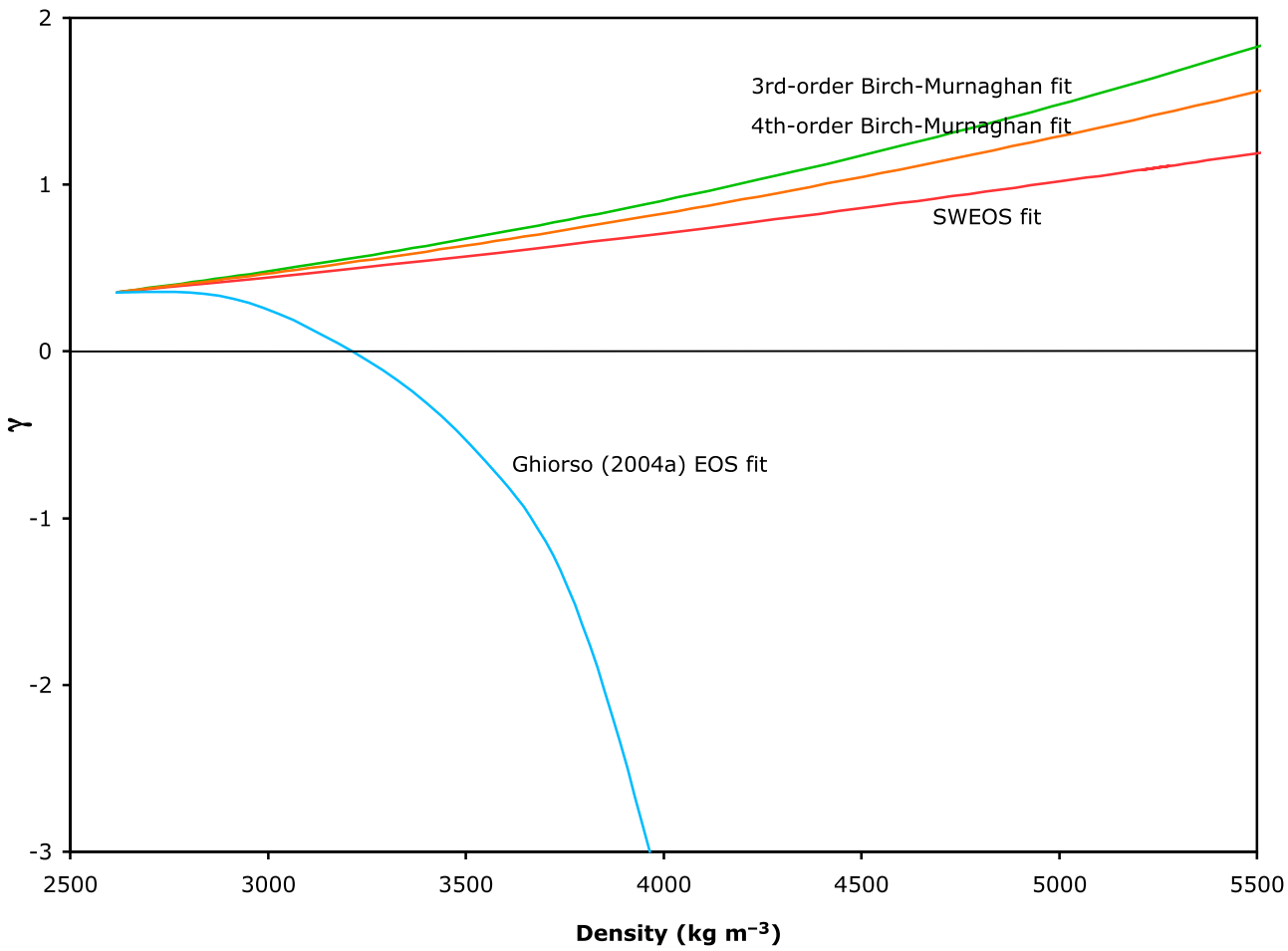

Figure 9. Density dependence of the Grüneisen parameter $\gamma(\rho)$ in four different thermal EOS fits for $Di_{64}An_{36}$ liquid.

to diverge more quickly with distance from the calibrated state points.

[65] We choose to illustrate the differences in prediction of off-Hugoniot states using the $Di_{64}An_{36}$ composition, since in this case we have a constraint on the thermal pressure in the SWEOS from the 300 K solid aggregate experiment. Recall from Figures 2 and 5 that all the formalisms considered appear to fit the high-temperature Hugoniot data equally well, though only the SWEOS exactly fits the 300 K solid aggregate shock datum. Figure 9 shows the dependence of the fitted Grüneisen parameters versus density for the four models. The SWEOS, 3rd-order and 4th-order BM/MG fits are all reasonably similar in this derivative parameter, having identical γ_o values and a range for q from −1.63 to −2.20. The GEOS shows very different $\gamma(\rho)$ behavior, with γ decreasing on compression, becoming negative at 3200 kg m^{-3}, and passing through a singularity to high positive values above ~4300 kg m^{-3}. Clearly this behavior is nonphysical and undesirable. It reflects the facts that γ is a derived parameter in the GEOS, with no a priori constraint on the form of its volume dependence, and that data lying only along the Hugoniot do not define this parameter well enough to ensure its stable behavior. This curve is plotted in Figure 9 not because we recommend using these values of γ but rather to illustrate some of the pitfalls inherent in the choice of EOS formalism.

[66] Figure 10 compares calculated 1673 K isotherms of $Di_{64}An_{36}$ liquid based on the four EOS fits presented in this paper and the original result of *Rigden et al.* [1988]. Near zero pressure, since the Hugoniot data are collected from an initial temperature of 1673 K, this isotherm is close to the Hugoniot and the ability of all these fits to match the Hugoniot is echoed in their closely similar predictions of density along the isotherm up to 24 GPa. Beyond this pressure they increasingly diverge. The *Rigden et al.* [1988] isotherm, as explained above, becomes essentially incompressible at a density of ~4000 kg m^{-3}, due to the kink inferred in U_s-u_p space in the original data set. The GEOS predicts lower isothermal density than the other fits. This can be interpreted in terms of the very large values of γ predicted at high density, which lead to a large offset between the Hugoniot and the isotherm. The remaining fits are more similar, but the differences become quite substantial at high pressure; for example the 3rd and 4th-order BM/MG fits differ in their predicted density by 9% at 140 GPa and 1673 K. This difference is much larger than the error in the measurement of density along the Hugoniot itself, and reflects the additional uncertainty that results from

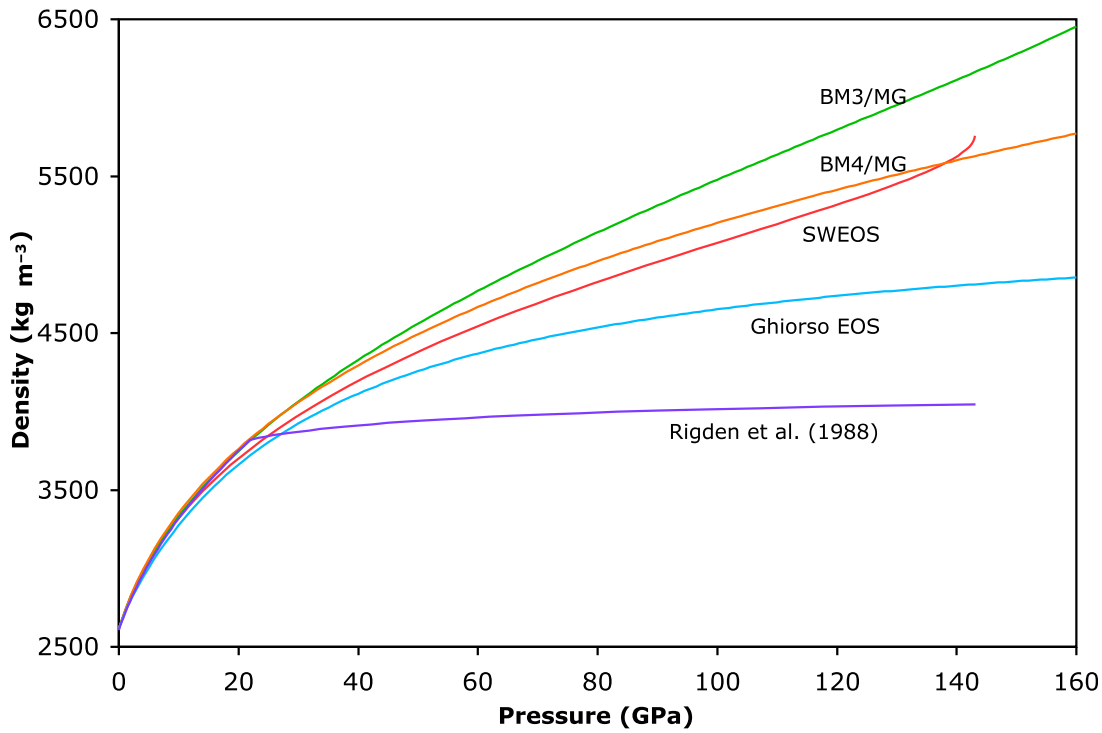

Figure 10. Computed density as a function of pressure along the 1673 K isotherm for five different thermal equations of state for $Di_{64}An_{36}$ liquid.

extrapolation away from the data using different thermal EOS formalisms. For many purposes — for instance, predicting the relative buoyancy of liquids and mantle solids at high pressure (see section 5.4 below) — the differences between these models may be unacceptably large. At this time, it is difficult to propose a satisfactory solution to this problem. Substantial progress in modeling, data collection, or both will be required to enable meaningful choice among EOS formalisms or the formulation of new, more rigorous and reliable formalisms [e.g., *de Koker and Stixrude*, 2009].

[67] The SWEOS model isotherm in Figure 10 is truncated at a maximum in pressure at 143 GPa. This is a consequence of the large value of γ at high density, together with the large temperature predicted along the Hugoniot for the constant C_V model adopted here. As Hugoniot temperature gets very high, the offset in pressure resulting from the Mie-Grüneisen correction down to 1673 K can overwhelm the increase in pressure along the Hugoniot and yield a predicted isotherm with a negative slope. However, in the absence of actual shock temperature data to constrain the behavior of C_V at high compression, this prediction carries little weight; it is an unsupported extrapolation far from available data.

5.3. Linear Mixing of Volumes

[68] Because naturally occurring silicate liquids are highly variable in composition, it is necessary, for many applications, to find reliable mixing rules for interpolating between sparsely sampled data on physical and chemical properties such as volumes, heat capacities, and enthalpies of mixing. Such mixing rules can in principle be arbitrarily complicated, but some very simple methods have been found accurate enough to fit large data sets. In particular, linear mixing of volumes is the cornerstone of the description of multi-component silicate liquids at ambient pressure. That is, if a liquid composition is a linear combination of a set of components, then the principle of linear mixing states that the volume (and all its derivatives) is given by the same linear combination of the volumes of the components [*Bottinga and Weill*, 1970]. An alternative statement is that the partial molar volumes of the end members are independent of composition. Linear mixing is the basis of the regressions of partial molar volume, thermal expansion, and compressibility given by *Lange and Carmichael* [1987; 1990] and *Lange* [1997], who also review the evidence for exceptions to linear mixing of volumes. Exceptions are known to occur in TiO_2-bearing liquids [e.g., *Dingwell*, 1992; *Gaetani et al.*, 2008; *Liu and Lange*, 2001; *Liu et al.*, 2007] and in oxidized liquids containing abundant Fe_2O_3 [e.g., *Dingwell and Brearley*, 1988; *Liu and Lange*, 2006], because these cations occupy different coordination environments in liquids of differing composition [e.g., *Farges et al.*, 1996; *Farges*, 1997; *Farges et al.*, 2004; *Henderson et al.*, 2003]. However, for the CaO-MgO-Al_2O_3-SiO_2 liquids studied in this work, the expectation from low-pressure studies of density, thermal expansion, and sound speed is that linear mixing of volume and its derivatives should hold. Indeed, we implicitly assume this relation at 1 bar, since the preheated density of our target liquids is derived from the *Lange* [1997] linear regression.

[69] It is unclear, however, whether linear mixing of volumes should hold at significantly elevated pressure. The fact that compositionally-dependent coordination changes of Ti^{4+} and Fe^{3+} lead to variations in their partial molar volumes at 1 bar strongly implies that any compositional dependence to pressure-induced coordination changes of

cations in silicate liquids will cause deviations from linear mixing. Indeed, the rate of coordination change of Al^{3+} and Si^{4+} with pressure has been studied using NMR spectroscopy of glasses quenched from pressure and is known to be compositionally dependent [*Allwardt et al.*, 2005; *Kelsey et al.*, 2009a; *Kelsey et al.*, 2009b; *Xue et al.*, 1991]. Furthermore, when pressure-explicit equations of state such as Birch-Murnaghan or Vinet are used to fit the volume of silicate liquids based on data sources such as sink-float experiments or fusion curves, strong compositional variations in K′ are found [*Agee*, 1992; *Ai and Lange*, 2008; *Lange*, 2003; 2007]. This also seems inconsistent with linear mixing of compressibility at elevated pressure.

[70] The three liquids considered in this study constitute one test of linear mixing, since the $Di_{64}An_{36}$ composition is a linear combination of the diopside and anorthite compositions. Despite expectations of possible complexity, *Rigden et al.* [1989] reported that, along isotherms calculated from their shock wave EOS fits, the volume of $Di_{64}An_{36}$ melt is predicted to within 1% by the appropriate mixture of the volumes of diopside and anorthite melts, up to 25 GPa. Beyond this pressure, the anomalous compression of $Di_{64}An_{36}$ melt (and only of this composition) that was inferred from the data of *Rigden et al.* [1988] causes a clear failure of linear mixing, increasing with increasing pressure beyond 25 GPa (Figure 11a). As discussed above (section 3.1), however, this anomaly is not confirmed by the present data, which leads us to re-examine the linear mixing hypothesis along this join in light of our new data.

[71] We note that, as usually formulated, linear mixing is tested by comparing the volumes of various compositions at equal pressure and temperature. Hence, the first step in making a linear mixing assessment using data collected along the Hugoniots of each liquid composition is correction of all the volumes to a common *P-T* curve. As discussed above in section 5.2, this exercise may add considerable uncertainty when the temperature extrapolation is large because of the choice of thermal EOS formalism and model parameters. The most conventional way to calculate this result is along the 1673 K isotherm, and we show this in Figure 11. In fact, this is an odd choice, since this isotherm lies below the liquidus of these compositions throughout the lower mantle and hence represents a metastable state. A much better constrained test is instead to correct all the Hugoniots to the calculated (not measured) *P-T* curve of the $Di_{64}An_{36}$ liquid Hugoniot rooted at 1673 K. This involves no thermal pressure correction for the intermediate composition and much smaller corrections for the end members. This comparison is shown in Figure 12, with the inset in Figure 12a showing the adopted *P-T* curve. We carry out the assessment of linear mixing for several choices of model. Panel (a) of Figures 11 and 12 shows the *Rigden et al.* [1988, 1989] models, which assume (γ/V) = constant, i.e. $q = 1$. This makes for very small thermal pressure terms, such that the *P-T* path selected makes little difference: Figures 11a and 12a, and the linear mixing deviation curves for Rigden models in Figures 11d and 12d, are almost indistinguishable. Panel (b) of Figures 11 and 12 shows the 3rd order BM/MG fits for all three compositions, including the segmented fit to anorthite, and also the 4th order BM/MG fit for anorthite that excludes the two *Rigden et al.* [1989] data points suspected of unrelaxed behavior. In this case the *P-T* path chosen makes a large difference to the result. Panel (c) of Figures 11 and 12 shows the *Ghiorso* [2004b] EOS fits, which again are quite sensitive to temperature. Whereas data and calculations elsewhere in this paper are reported in terms of density, for this purpose we use molar volume.

[72] At low pressure, all the choices of EOS suggest that the volume of the intermediate composition can be predicted from the volumes of the end members to within 2% from ambient pressure (where such a relation is assumed) up to ~20 GPa. This in itself remains a notable result, and useful for modeling of liquid densities under upper mantle conditions. However, beyond this pressure the situation becomes complicated. Every model we consider shows rapidly increasing deviation from the ideal model beyond 20 GPa when plotted along the 1673 K isotherm (Figure 11d). In each case, the reason for such deviation is different. In the original Rigden fits (Figure 11a), it is due to anomalous incompressibility of the intermediate composition. With the BM3/MG fits from this work (Figure 11b), it is initially due instead to the anomalous compression of anorthite liquid described in section 4.4. At higher pressure it appears to be the large thermal pressure correction for $Di_{64}An_{36}$ that dominates. With the GEOS (Figure 11c), it is not obvious which composition is anomalous; we can only observe that the compressibility does not mix linearly and so the volumes diverge from linear mixing at high pressure.

[73] When assessed along the model *P-T* curve of the $Di_{64}An_{36}$ Hugoniot, the Rigden models still fail to show linear mixing above 24 GPa due to the anomalous incompressibility of the intermediate composition (Figure 12a). The Ghiorso EOS again deviates strongly from linear mixing above ~20 GPa, but in this case the composition causing anomalous behavior is clearly diopside, whose thermal pressure correction is large enough to yield negative $(dV/\partial P)$ at high pressure along this *P-T* curve. However, the BM/MG fits satisfy linear mixing to within 2% at all mantle pressures, when assessed along this high-temperature curve (Figure 12b and 12d). This is true both with the compound anorthite and with the 4th order anorthite model excluding the two suspicious data points.

[74] The apparent success of linear mixing along the diopside-anorthite join, using the BM/MG fits along the Hugoniot *P-T* curve, is remarkable, but the significance of this result is unclear. For application to problems in the lower mantle, except possibly during the earliest stages of magma ocean evolution, it is necessary to evaluate liquid densities at substantially lower temperature than were used in Figure 12. But we cannot say whether the deviation from linear mixing along the isotherm (Figure 11) is actually constrained by the current models or is merely an artifact of poorly-defined thermal pressure terms and the large temperature correction applied. With further experiments off the pre-heated liquid Hugoniot of each composition, constraints on the correct form and parameters of the thermal pressure term may emerge, and this question may become resolvable. Meanwhile, as an interim statement, it may be that the failure of linear mixing along the isotherm for this particular join results from coordination changes specifically in anorthite liquid that occur differently from those in diopside or $Di_{64}An_{36}$ liquid. We have speculated that the anomalous behavior of anorthite liquid when fitted to all data, as well as

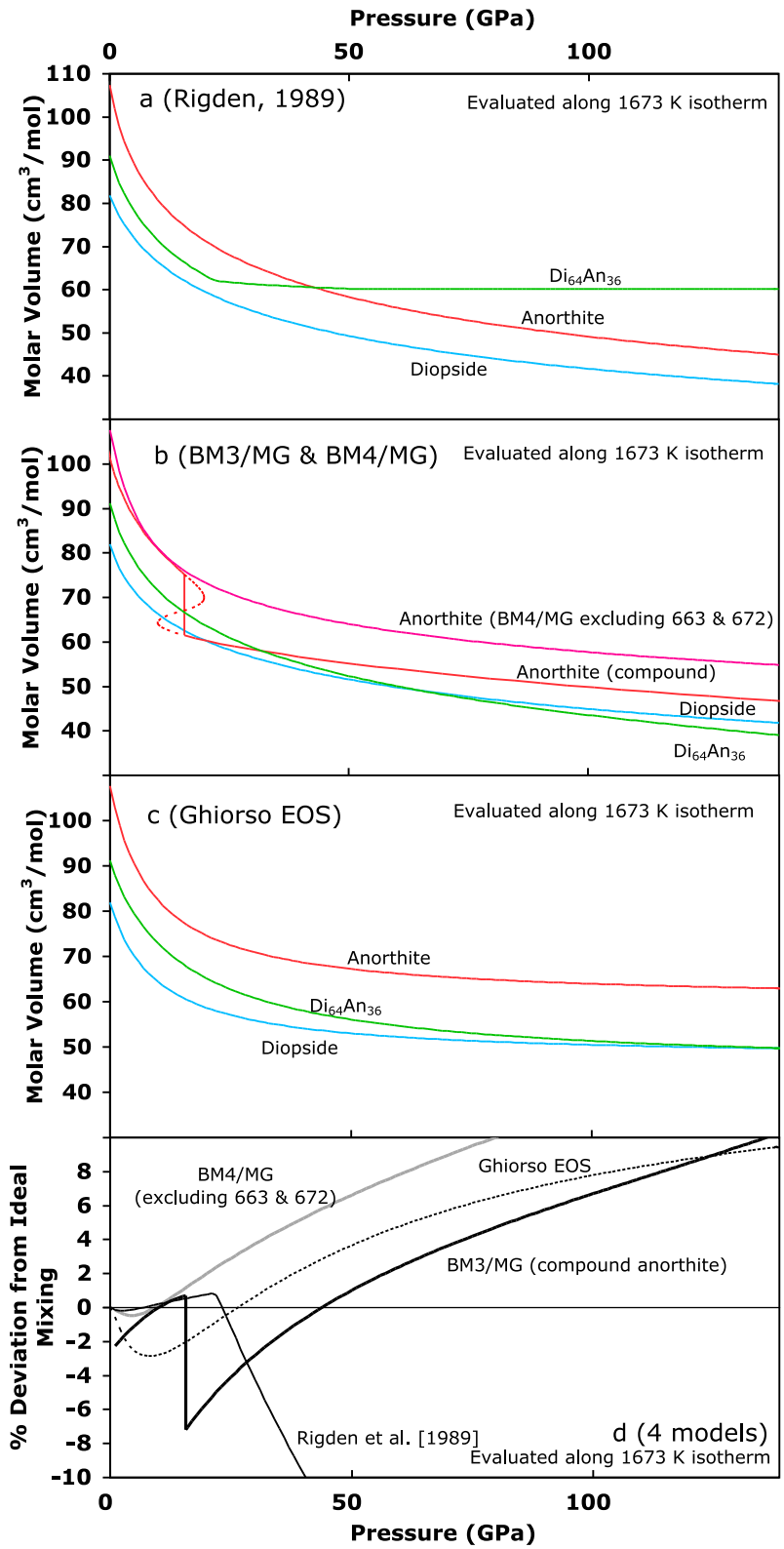

Figure 11. Assessments of linear mixing along the anorthite-diopside join and the 1673 K isotherm. (a) The EOS fits of *Rigden et al.* [1989]. (b) The BM/MG fits to the combined data set of this work. For Anorthite, both the compound fit to the entire data set and the 4th-order fit to the data excluding two experiments of *Rigden et al.* [1989] are shown. (c) The GEOS fits to the combined data sets. (d) The deviation from the prediction of ideal mixing, for each of the models presented in (a), (b), and (c), as a percent difference between the molar volume of $Di_{64}An_{36}$ liquid and $0.64*V_{diopside} + 0.36*V_{anorthite}$ at equal P and T.

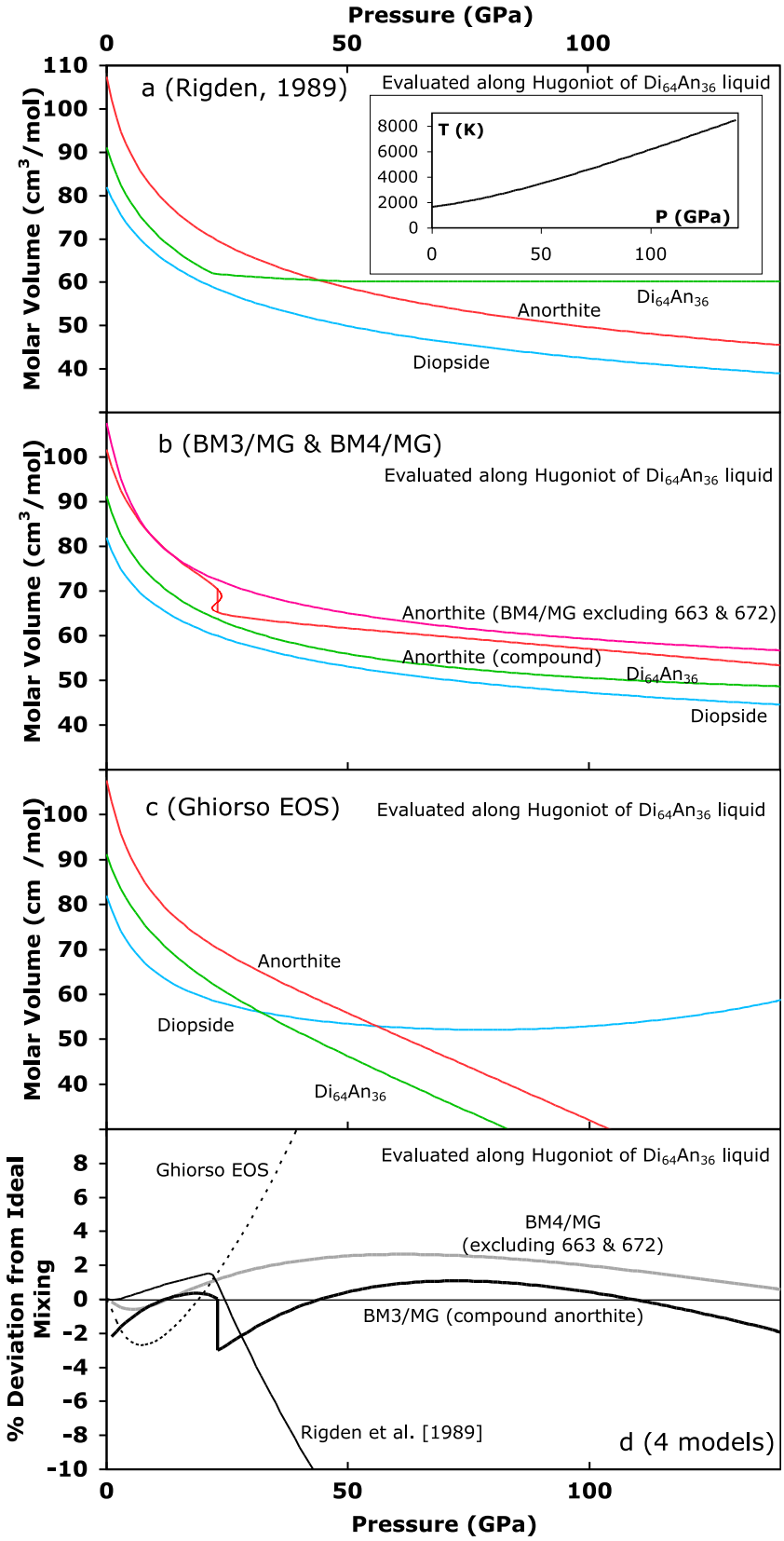

Figure 12. Assessments of linear mixing along the anorthite-diopside join and the computed *P-T* path of the $Di_{64}An_{36}$ liquid Hugoniot. All symbols as in Figure 11. The inset to part (a) shows the adopted *P-T* path for this comparison, reaching ~9000 K at 140 GPa.

the possible failure of some of the anorthite experiments to relax upon shock compression, are due to its fully polymerized network character. Hence it remains quite possible that linear mixing at lower mantle temperatures will be an adequate description of the compositional dependence of the volumes of the much less polymerized liquids that are actually expected to arise in the mantles of terrestrial planets at high pressure. This remains a question for future work that characterizes the EOS of more mafic liquids, with sufficient coverage of composition space that some compositions are linear combinations of others in the data set.

5.4. Compression Mechanisms in Silicate Melts

[75] Changes in macroscopic density of silicate liquids in response to applied pressure and temperature are accommodated at the microscopic level by a variety of mechanisms, including bond shortening, bond bending, network topology adjustment, and coordination change. Although data on the EOS are sensitive to the aggregate result of all these microscopic phenomena, different kinds of data that probe the liquid at spatial scales of 10^{-10} to 10^{-8} m and temporal scales of 10^{-12} to 10^{-6} s are necessary to observe compression mechanisms directly. Much work has indeed focused on such measurements using a variety of spectroscopic and diffraction-related techniques, both on quenched glasses and *in situ* on liquids at high pressure and temperature [the subject of such observations is reviewed in *Mysen and Richet*, 2005; *Stebbins et al.*, 1995]. Microscopic mechanisms can also be interrogated with molecular dynamics calculations [e.g., *Karki et al.*, 2006; *Spera et al.*, 2009], wherein the positions and momenta of all atoms are calculated as functions of time. Although this paper reports only macroscopic information, we nevertheless consider here the implications for microscopic compression mechanisms.

[76] There is general consensus that bond bending and network topology are important mechanisms, especially in highly polymerized liquids and at low (≤1 GPa) pressure [*Gaetani et al.*, 1998; *Guillot and Sator*, 2007; *Lange*, 2003; 2007; *Stixrude and Bukowinski*, 1989]. There is also general consensus that coordination change is essential to achieving densities comparable to high-pressure solid polymorphs and should be the dominant mechanism at significantly elevated pressure (≥3 GPa) [*Allwardt et al.*, 2005; *Farber and Williams*, 1992; *Stixrude and Karki*, 2005]. Important issues that remain unresolved are the relationship between network topologies and coordination numbers and the width of the statistical distribution of coordination numbers. The anomalous decrease in compressibility observed in the *Rigden et al.* [1988] data on $Di_{64}An_{36}$ liquid was interpreted by *Stolper and Ahrens* [1987] with a model whereby gradual bond bending of a tetrahedral network effected a transition to octahedral coordination. In this non-statistical model, all the Si cations in the network pass through a gradual coordination transition together, and the distribution of coordination numbers at any pressure remains narrow. Such a model is characterized by a sudden decrease in compressibility when the bending and topological degrees of freedom are exhausted, with the liquid becoming similar in structure and bulk modulus to octahedrally coordinated solid phases. Molecular dynamics simulations, on the other hand, tend to show that each Si or Al cation remains in a relatively low-distortion 4-, 5-, 6- or higher-coordinated polyhedron and that bulk densification of the melt is better described by a gradual shift in the mean coordination number through changes in the statistical population of these polyhedral units [*Stixrude and Karki*, 2005]. In such a model, sudden changes in compressibility are unexpected, as the broad distribution of coordination numbers around individual cations can accommodate smooth compression through population shifts.

[77] The results in this paper suggest that both views have merit, and that the best view of compression in a given liquid composition varies among liquid compositions. In particular, the regular 3rd-order compression (linear Hugoniot) observed for diopside and $Di_{64}An_{36}$ liquids is consistent with gradual coordination change from ambient-pressure structures all the way to densities similar to lower mantle phases, without sudden compression anomalies. This behavior suggests that at microscopic scale there is likely also to be a broad distribution of coordination numbers at each particular pressure. The failure of the compression anomaly seen by *Rigden et al.* [1988] to extrapolate to lower-mantle pressure removes much of the motivation to apply a model like *Stolper and Ahrens* [1987] to this composition. On the other hand, the complex behavior of anorthite liquid in our shock compression data and in the molecular dynamics simulations of *Spera et al.* [2009] suggests that this composition may experience distinctive low-pressure compression mechanisms, relatively sudden shifts in compression mechanism, and the possibility of abrupt changes in coordination number over small pressure ranges. It is also possible that its equilibrium behavior is not so anomalous and that shock wave experiments on anorthite between 26 and ~36 GPa are misleading due to unrelaxed behavior, perhaps as discussed above specifically unrelaxed with respect to thermal expansion modes. Along the compositional join studied in this work, anorthite occupies the end of the spectrum representing the most polymerized compositions. It is a fully-networked liquid with zero non-bridging oxygens [*Mysen and Richet*, 2005]. A reasonable speculation is that some population of network-modifying cations are necessary to provide enough topological degrees of freedom to enable statistical coordination shift and smooth compression behavior. If this is correct, we predict that mafic to ultramafic liquid compositions should, in general, display smooth compression behavior in experimental and theoretical studies. Furthermore, such behavior may be more consistent with linear mixing of volumes among such mafic to ultramafic compositions and with the eventual development of a simple framework for the systematic prediction of their densities as functions of pressure, temperature, and composition.

5.5. Density of Melts Relative to Lower Mantle Solids

[78] One of the primary motivations behind the study of silicate liquid equations of state relates to the role of liquid buoyancy in driving melt-solid segregation and hence chemical differentiation of the planet. In this regard, the occurrence of density crossovers, or pressures above which silicate liquids are denser than coexisting solids, is a critical issue [*Agee and Walker*, 1987; 1988; 1993; *Agee*, 1998; *Rigden et al.*, 1984; *Stolper et al.*, 1981; *Walker et al.*, 1988]. Upon cooling of a magma chamber or magma ocean, density crossovers between the bulk liquid and near-

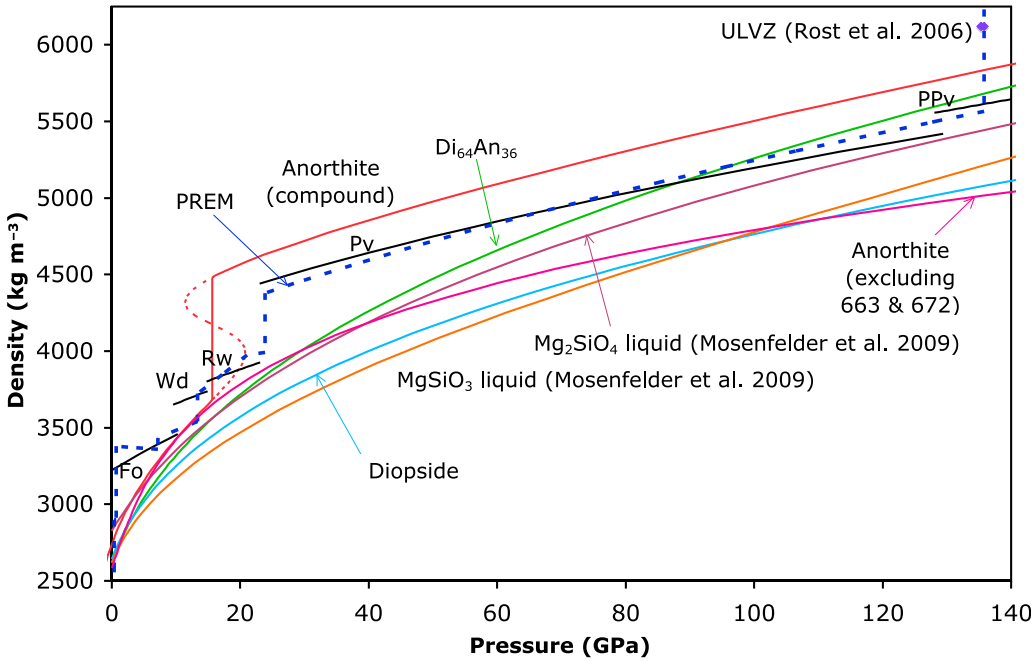

Figure 13. Computed density as a function of pressure along a plausible mantle geotherm with foot temperature 1673 K; *T* increases to 3073 K at 140 GPa; no thermal boundary layers are included at top or bottom of the mantle. Shown are five Fe-free silicate liquids (two candidate models for Anorthite liquid) and major Fe-free mantle minerals. Mineral equations of state for forsterite (Fo), wadsleyite (Wd) and ringwoodite (Rw) are from *Stixrude and Lithgow-Bertelloni* [2005]; those for perovskite (Pv) and postperovskite (PPv) are from *Mosenfelder et al.* [2009]. Also shown are the lower mantle density profile from PREM [*Dziewonski and Anderson*, 1981] and the density of the ULVZ inferred from reflection coefficients [*Rost et al.*, 2006].

liquidus solid phases delimit regions where early-formed crystals will float upwards from those where they will sink downwards, affecting the formation of cumulus rocks at the top or bottom of a magma chamber and the geochemical consequences of differentiation of a magma ocean. On the other hand, during partial melting, density crossovers between the bulk residual solid rock and near-solidus liquid compositions separate cases where melt will segregate upwards, perhaps intruding the crust or erupting at the surface, from cases where melt will segregate downwards, perhaps to accumulate at one or more internal density boundaries within the earth such as the transition zone or core-mantle boundary. In this comparison it is important to consider the changing chemical composition of liquids equilibrated with mantle solids with increasing pressure. A discussion of liquid buoyancy can either consider fixed liquid compositions, equilibrated liquid compositions in restricted subsystems such as the olivine binary, or fully equilibrated multi-component liquids.

[79] A range of basaltic liquids are denser at the base of the upper mantle than the major upper mantle solid, olivine, or a model mantle assemblage of olivine, pyroxenes, and garnet (at equilibrium distribution of Fe and Mg). The transition zone to the lower mantle, however, is marked by changes in the solid assemblage to major phases that are denser than known liquids. It is not yet firmly established whether continued compression through the lower mantle eventually yields basaltic liquids denser than the lower mantle. In this regard, the sudden decrease in compressibility of $Di_{64}An_{36}$ basalt analogue liquid at 25 GPa described by *Rigden et al.* [1988] was quite significant because it implied that basaltic liquids in the lower mantle are no more compressible than solids, and would remain positively buoyant at all mantle pressures.

[80] In Figure 13, we compare the densities of the three silicate liquids whose thermal EOS we have constrained here, as well as forsterite and enstatite liquids [*Mosenfelder et al.*, 2009] to the densities of mantle minerals. Since thermal expansion of solid and liquids are different, the temperature or thermal gradient at which we do this comparison is significant; we have chosen to show densities along a plausible modern mantle adiabat, with a potential temperature of 1673 K and a gradient of 10 K/GPa. This calculation applies to the bulk of the modern mantle, but not to the thermal boundary layer just above the core. Once again, this comparison is sensitive to the errors introduced in making thermal pressure corrections by the uncertainty in the form and parameters of the thermal EOS (see Figures 10–12 and section 5.2). The comparison in Figure 13 is done with 3rd-order BM/MG fits for all the solid phases, for diopside and for $Di_{64}An_{36}$ liquid; with both the compound 3rd-order BM/MG fit and the 4th-order BM/MG fit excluding suspicious data for anorthite liquid; and with the 4th-order BM/MG fits of *Mosenfelder et al.* [2009] for $MgSiO_3$ and Mg_2SiO_4 liquids. Since our olivine, pyroxene, and basalt analogue compositions are Fe-free, the most suitable comparison is to the Fe-free end members of mantle solid solutions. In fact, it has long been known [*Anderson*,

1968] and recently confirmed [*Ricolleau et al.*, 2009] that Fe-free $MgSiO_3$ perovskite provides a reasonable match to the actual density profile of the lower mantle. Nevertheless we emphasize that none of the liquid compositions considered is in equilibrium with a mantle assemblage at elevated pressure.

[81] Evidently, only the compound anorthite model liquid and the $Di_{64}An_{36}$ liquid are predicted to reach densities exceeding those of major lower mantle phases, and of these only $Di_{64}An_{36}$ liquid has a reasonably well-constrained thermal EOS fit. If $Di_{64}An_{36}$ liquid were present in the ULVZ, it would appear to be gravitationally stable relative to model solids or PREM (although that comparison should be done at the core-mantle boundary temperature, not on the extension of the lower mantle isentrope), but the density contrast is not quite enough to satisfy the constraint from reflectivity studies that the density jump at the ULVZ be 5–10% [*Rost et al.*, 2006].

[82] The effect of Fe on density crossovers is often presented as a simple matter. In all known cases, when Fe and Mg are both present, Fe partitions preferentially into the melt phase in the sense that the Fe/Mg ratio of the melt is higher (often by about a factor of three) than that of the coexisting solid [*Bowen and Schairer*, 1935; *Mibe et al.*, 2006; *Trønnes et al.*, 1992], which ought to increase the liquid density relative to the solid. Hence, allowing only Fe/Mg-exchange equilibrium but no other chemical changes in the liquid composition, the liquid densities in the Fe-bearing system will be higher, relative to the solids, than shown in Figure 13, and density crossovers easier to achieve at lower pressure [*Stixrude and Karki*, 2005; *Stixrude et al.*, 2009]. This exercise is artificial, however, because the liquids being considered here are not in overall chemical equilibrium with lower mantle solids and, in fact, the equilibrium relations are unknown at these conditions. In particular, not only the Fe/Mg ratios but also the absolute FeO contents of liquids in equilibrium with mantle solids need to be assessed to calculate densities. Under upper mantle conditions, MgO is strongly compatible (concentrated in the solid phases), where FeO has a bulk partition coefficient close to unity [see, e.g. *Langmuir et al.*, 1992], which suggests that addition of FeO would not have a major effect on melt buoyancy. In practice, determining liquid buoyancy in the lower mantle requires, first, deciding whether to examine fixed or equilibrated liquid compositions; second, for the equilibrated case, suitable phase equilibrium or partitioning data; and, third, data on the densities of Fe-bearing liquids under lower mantle conditions, which are presently lacking. Data on the EOS of fayalite (Fe_2SiO_4) liquid up to modest pressures (static data to 6 GPa, shock wave to 47 GPa) are presently contradictory [*Agee*, 1992; *Chen et al.*, 2002]. More data on Fe-bearing liquids, including a wider range of compositions and extension to higher pressure, are needed before the issue of liquid buoyancy in Fe-bearing mantle systems can be settled.

[83] In spite of our present very limited understanding of the effects of iron on the lowermost mantle melts, our current data set resolves a large effect of Ca and Al on the high-pressure EOS of molten silicates. Although ultramafic liquids are probably positively buoyant, it appears that melts of basaltic composition may be negatively buoyant in the lower mantle and could promote the downward differentiation of Ca and Al as well as other geochemically significant incompatible elements (e.g. U, Th, K, Sm, Nd, and Xe). One physical setting where such differentiation may have operated is during crystallization of a primordial whole-mantle magma ocean, leading to an isolated enriched basal reservoir such as that discussed by *Labrosse et al.* [2007].

[84] **Acknowledgments.** This paper has taken many years of sustained effort by our irreplaceable technical staff: Michael Long, Eprapodito Gelle and Russel Oliver. Yongqin Jiao contributed to the very early stages and Daoyuan Sun made substantial contributions to the middle stage of the effort. Jed Mosenfelder provided the anorthite glass sample and frequent advice. Mark Ghiorso kindly carried out the fits of this data to his EOS formalism and shared prepublication results of his work with Frank Spera. This work was supported by the U. S. National Science Foundation through awards EAR-0207934, EAR-0409785, EAR-0552009, EAR-0555685, EAR-0609804 and EAR-0810116.

References

Adjaoud, O., G. Steinle-Neumann, and S. Jahn (2008), Mg_2SiO_4 liquid under high pressure from molecular dynamics, *Chem. Geol.*, *256*(3–4), 185–192, doi:10.1016/j.chemgeo.2008.06.031.

Agee, C. B. (1992), Isothermal compression of molten Fe_2SiO_4, *Geophys. Res. Lett.*, *19*, 1169–1172.

Agee, C. B. (1998), Crystal-liquid density inversions in terrestrial and lunar magmas, *Phys. Earth. Planet. Int.*, *107*(1–3), 63–74.

Agee, C. B. (2008), Compressibility of water in magma and the prediction of density crossovers in mantle differentiation, *Philos. Trans. R. Soc. Ser. A*, *366*(1883), 4239–4252, doi:10.1098/Rsta.2008.0071.

Agee, C. B., and D. Walker (1987), Olivine flotation in a chondritic mantle, *Meteoritics*, *22*(4), 314–314.

Agee, C. B., and D. Walker (1988), Static compression and olivine flotation in ultrabasic silicate liquid, *J. Geophys. Res.*, *93*(B4), 3437–3449.

Agee, C. B., and D. Walker (1993), Olivine flotation in mantle melt, *Earth Planet. Sci. Lett.*, *114*(2–3), 315–324.

Ai, Y. H., and R. A. Lange (2008), New acoustic velocity measurements on CaO-MgO-Al_2O_3-SiO_2 liquids: Reevaluation of the volume and compressibility of $CaMgSi_2O_6$-$CaAl_2Si_2O_8$ liquids to 25 GPa, *J. Geophys. Res.*, *113*, B04203, doi:10.1029/2007JB005010.

Akins, J. A., and T. J. Ahrens (2002), Dynamic compression of SiO_2: A new interpretation, *Geophys. Res. Lett.*, *29*(10), 1394, doi:10.1029/2002GL014806.

Akins, J. A., S.-N. Luo, P. D. Asimow, and T. J. Ahrens (2004), Shock-induced melting of $MgSiO_3$ perovskite and implications for melts in Earth's lowermost mantle, *Geophys. Res. Lett.*, *31*, L14612, doi:10.1029/2004GL020237.

Albarède, F., and J. Blichert-Toft (2007), The split fate of the early Earth, Mars, Venus, and Moon, *Comptes Rendus Geoscience*, *339*(14–15), 917–927, doi:10.1016/j.crte.2007.09.006.

Allègre, C. J., G. Manhès, and C. Göpel (1995), The Age of the Earth, *Geochim. Cosmochim. Acta*, *59*(8), 1445–1456.

Allwardt, J. R., J. F. Stebbins, B. C. Schmidt, D. J. Frost, A. C. Withers, and M. M. Hirschmann (2005), Aluminum coordination and the densification of high-pressure aluminosilicate glasses, *Am. Min.*, *90*(7), 1218–1222, doi:10.2138/Am.2005.1836.

Anderson, D. L. (1968), Chemical inhomogeneity of mantle, *Earth Planet. Sci. Lett.*, *5*(2), 89–94.

Asimow, P. D., D. Sun, and T. J. Ahrens (2008), Shock compression of preheated Molybdenum to 300 GPa, *Phys. Earth. Planet. Int.*, *174*, 302–308, doi:10.1016/j.pepi.2008.08.004.

Batsanov, S. S. (1994), *Effects of Explosions on Materials: Modification and Synthesis Under High-Pressure Shock Compression*, 194 pp., Springer, Berlin.

Baxter, E. F., P. D. Asimow, and K. A. Farley (2007), Grain boundary partitioning of Ar and He, *Geochim. Cosmochim. Acta*, *71*(2), 434–451, doi:10.1016/J.Gca.2006.09.011.

Bottinga, Y., and D. F. Weill (1970), Densities of silicate liquid systems calculated from partial molar volumes of oxide components, *Am. J. Sci.*, *269*, 169–182.

Bowen, N. L., and J. F. Schairer (1935), The system, MgO-FeO-SiO_2, *Am. J. Sci.*, *29*(170), 151–217.

Brown, J. M., M. D. Furnish, and R. G. McQueen (1987), Thermodynamics for $(Mg,Fe)_2SiO_4$ from the Hugoniot, in *High-Pressure Research in*

Mineral Physics, edited by M. H. Manghnani and Y. Syono, pp. 373–384, AGU, Washington, D. C.

Canup, R. M. (2004), Simulations of a late lunar-forming impact, *Icarus*, *168*(2), 433–456.

Chen, G. Q., and T. J. Ahrens (1998), Radio frequency heating coils for shock wave experiments, in *High-Pressure Materials Research*, edited by R. M. Wentzcovitch et al., pp. 63–71, Materials Research Society, Warrendale, PA.

Chen, G. Q., T. J. Ahrens, and E. M. Stolper (2002), Shock-wave equation of state of molten and solid fayalite, *Phys. Earth. Planet. Int.*, *134*(1–2), 35–52.

de Koker, N. (2010), Structure, thermodynamics, and diffusion in $CaAl_2Si_2O_8$ liquid from first-principles molecular dynamics, *Geochim. Cosmochim. Acta.*, *74*(19), 5657–5671, doi:10.1016/j.gca.2010.02.024.

de Koker, N., and L. Stixrude (2009), Self-consistent thermodynamic description of silicate liquids, with application to shock melting of MgO periclase and $MgSiO_3$ perovskite, *Geophys. J. Int.*, *178*(1), 162–179, doi:10.1111/j.1365-246X.2009.04142.x.

de Koker, N. P., L. Stixrude, and B. B. Karki (2008), Thermodynamics, structure, dynamics, and freezing of Mg_2SiO_4 liquid at high pressure, *Geochim. Cosmochim. Acta*, *72*(5), 1427–1441, doi:10.1016/J.Gca.2007.12.019.

Dingwell, D. B. (1992), Density of some titanium-bearing silicate liquids and the compositional dependence of the partial molar volume of TiO2, *Geochim. Cosmochim. Acta*, *56*(9), 3403–3407.

Dingwell, D. B. (1995), Relaxation in silicate melts: Some applications, *Structure, Dynamics and Properties of Silicate Melts*, *32*, 21–66.

Dingwell, D. B., and M. Brearley (1988), Melt densities in the CaO-FeO-Fe_2O_3-SiO_2 system and the compositional dependence of the partial molar volume of Ferric Iron in silicate melts, *Geochim. Cosmochim. Acta*, *52*(12), 2815–2825.

Dziewonski, A. M., and D. L. Anderson (1981), Preliminary reference earth model, *Phys. Earth. Planet. Int.*, *25*(4), 297–356.

Efron, B. (1982), *The Jackknife, the Bootstrap, and Other Resampling Plans*, 92 pp., Soc. for Ind. and Appl. Math., Philadelphia, PA.

Elkins-Tanton, L. T., P. C. Hess, and E. M. Parmentier (2005), Possible formation of ancient crust on Mars through magma ocean processes, *J. Geophys. Res.*, *110*, E12S01, doi:10.1029/2005JE002480.

Farber, D. L., and Q. Williams (1992), Pressure-induced coordination changes in alkali-germanate melts – An *in situ* spectroscopic investigation, *Science*, *256*(5062), 1427–1430.

Farges, F. (1997), Coordination of Ti^{4+} in silicate glasses: A high-resolution XANES spectroscopy study at the Ti K edge, *Am. Min.*, *82*(1–2), 36–43.

Farges, F., G. E. Brown, A. Navrotsky, H. Gan, and J. R. Rehr (1996), Coordination chemistry of Ti(IV) in silicate glasses and melts.3. Glasses and melts from ambient to high temperatures, *Geochim. Cosmochim. Acta*, *60*(16), 3055–3065.

Farges, F., Y. Lefrère, S. Rossano, A. Berthereau, G. Calas, and G. E. Brown (2004), The effect of redox state on the local structural environment of iron in silicate glasses: a molecular dynamics, combined XAFS spectroscopy, and bond valence study, *Journal of Non-Crystalline Solids*, *344*(3), 176–188, doi:10.1016/J.Jnoncrysol.2004.07.050.

Gaetani, G. A., P. D. Asimow, and E. M. Stolper (1998), Determination of the partial molar volume of SiO_2 in silicate liquids at elevated pressures and temperatures: A new experimental approach, *Geochim. Cosmochim. Acta*, *62*, 2499–2508.

Gaetani, G. A., P. D. Asimow, and E. M. Stolper (2008), A model for rutile saturation in silicate melts with applications to eclogite partial melting in subduction zones and mantle plumes, *Earth Planet. Sci. Lett.*, *272*(3–4), 720–729, doi:10.1016/J.epsl.2008.06.002.

Garnero, E. J., and D. V. Helmberger (1995), A very slow basal layer underlying large-scale low-velocity anomalies in the lower mantle beneath the Pacific - Evidence from core phases, *Phys. Earth. Planet. Int.*, *91*(1–3), 161–176.

Garnero, E. J., and D. V. Helmberger (1996), Seismic detection of a thin laterally varying boundary layer at the base of the mantle beneath the central-Pacific, *Geophys. Res. Lett.*, *23*(9), 977–980.

Ghiorso, M. S. (2004a), An equation of state for silicate melts. III. Analysis of stoichiometric liquids at elevated pressure: Shock compression data, molecular dynamics simulations and mineral fusion curves, *Am. J. Sci.*, *304*(8–9), 752–810.

Ghiorso, M. S. (2004b), An equation of state for silicate melts. I. Formulation of a general model, *Am. J. Sci.*, *304*(8–9), 637–678.

Ghiorso, M. S., and R. O. Sack (1995), Chemical mass transfer in magmatic processes IV. A revised and internally consistent thermodynamic model for the interpolation and extrapolation of liquid-solid equilibria in magmatic systems at elevated temperatures and pressures, *Contrib. Mineral. Petrol.*, *119*, 197–212.

Ghiorso, M. S., D. Nevins, I. Cutler, and F. J. Spera (2009), Molecular dynamics studies of $CaAl_2Si_2O_8$ liquid. Part II: Equation of state and a thermodynamic model, *Geochim. Cosmochim. Acta*, *73*(22), 6937–6951, doi:10.1016/J.Gca.2009.08.012.

Ghosh, S., E. Ohtani, K. Litasov, A. Suzuki, and T. Sakamaki (2007), Stability of carbonated magmas at the base of the Earth's upper mantle, *Geophys. Res. Lett.*, *34*, L22312, doi:10.1029/2007GL031349.

Guillot, B., and N. Sator (2007), A computer simulation study of natural silicate melts. Part II: High pressure properties, *Geochim. Cosmochim. Acta*, *71*(18), 4538–4556, doi:10.1016/j.gca.2007.05.029.

Hawke, R. S., A. R. Susoeff, and D. W. Greenwood (1995), Design considerations for a passive magnetic induction signal generator for sensing hypervelocity projectile passage, *IEEE Transactions on Magnetics*, *31*, 925–926.

Henderson, G. S., X. Y. Liu, and M. E. Fleet (2003), Titanium coordination in silicate glasses investigated using O K-edge X-ray absorption spectroscopy, *Mineralogical Magazine*, *67*(4), 597–607, doi:10.1180/0026461036740120.

Hernlund, J. W., and P. J. Tackley (2007), Some dynamical consequences of partial melting in Earth's deep mantle, *Phys. Earth. Planet. Int.*, *162*(1–2), 149–163.

Hirschmann, M. M. (2006), Water, melting, and the deep Earth H_2O cycle, *Ann. Rev. Earth Planet. Sci.*, *34*, 629–653, doi:10.1146/Annurev.Earth.34.031405.125211.

Hixson, R. S., D. A. Boness, J. W. Shaner, and J. A. Moriarty (1989), Acoustic velocities and phase transitions in molybdenum under strong shock compression, *Phys. Rev. Lett.*, *62*(6), 637–640.

Hutchison, R. (1992), Earliest planetary melting – The view from meteorites, *J. Volcanol. Geotherm. Res.*, *50*(1–2), 7–16.

Jackson, I., and T. J. Ahrens (1979), Shock-wave compression of single crystal forsterite, *J. Geophys. Res.*, *84*, 3039–3048.

Jeanloz, R. (1989), Shock-wave equation of state and finite strain theory, *J. Geophys. Res.*, *94*(B5), 5873–5886.

Karki, B. B., D. Bhattarai, and L. Stixrude (2006), A first-principles computational framework for liquid mineral systems, *Cmc-Computers Materials & Continua*, *3*(3), 107–117.

Kelsey, K. E., J. F. Stebbins, J. L. Mosenfelder, and P. D. Asimow (2009a), Simultaneous aluminum, silicon, and sodium coordination changes in 6 GPa sodium aluminosilicate glasses, *Am. Min.*, *94*(8–9), 1205–1215, doi:10.2138/Am.2009.3177.

Kelsey, K. E., J. F. Stebbins, D. M. Singer, G. E. Brown, J. L. Mosenfelder, and P. D. Asimow (2009b), Cation field strength effects on high pressure aluminosilicate glass structure: Multinuclear NMR and La XAFS results, *Geochim. Cosmochim. Acta*, *73*(13), 3914–3933, doi:10.1016/J.Gca.2009.03.040.

Labrosse, S., J. W. Hernlund, and N. Coltice (2007), A crystallizing dense magma ocean at the base of the Earth's mantle, *Nature*, *450*(7171), 866–869.

Lange, R. A. (1997), A revised model for the density and thermal expansivity of K_2O-Na_2O-CaO-MgO-Al_2O_3-SiO_2 liquids from 700 to 1900 K: Extension to crustal magmatic temperatures, *Contrib. Mineral. Petrol.*, *130*(1), 1–11.

Lange, R. A. (2003), The fusion curve of albite revisited and the compressibility of $NaAlSi_3O_8$ liquid with pressure, *Am. Min.*, *88*(1), 109–120.

Lange, R. A. (2007), The density and compressibility of $KAlSi_3O_8$ liquid to 6.5 GPa, *Am. Min.*, *92*(1), 114–123, doi:10.2138/Am.2007.2246.

Lange, R. A., and I. S. E. Carmichael (1987), Densities of Na_2O-K_2O-CaO-MgO-FeO-Fe_2O_3-Al_2O_3-TiO_2-SiO_2 liquids - New measurements and derived partial molar properties, *Geochim. Cosmochim. Acta*, *51*(11), 2931–2946.

Lange, R. A., and A. Navrotsky (1992), Heat-capacities of Fe_2O_3-bearing silicate liquids, *Contrib. Mineral. Petrol.*, *110*(2–3), 311–320.

Lange, R. L., and I. S. E. Carmichael (1990), Thermodynamic properties of silicate liquids with emphasis on density, thermal expansion and compressibility, in *Modern Methods of Igneous Petrology: Understanding Magmatic Processes*, edited by J. Nicholls and J. K. Russell, pp. 25–64, Mineralogical Society of America, Washington, D. C.

Langmuir, C. H., E. M. Klein, and T. Plank (1992), Petrological systematics of mid-ocean ridge basalts: Constraints on melt generation beneath ocean ridges, in *Mantle Flow and Melt Generation at Mid-Ocean Ridges*, edited by J. Phipps Morgan et al., pp. 183–280.

Lay, T., E. J. Garnero, and Q. Williams (2004), Partial melting in a thermo-chemical boundary layer at the base of the mantle, *Phys. Earth. Planet. Int.*, *146*(3–4), 441–467, doi:10.1016/j.pepi.2004.04.004.

Liu, Q., and R. A. Lange (2001), The partial molar volume and thermal expansivity of TiO_2 in alkali silicate melts: Systematic variation with Ti coordination, *Geochimica et Cosmochimica Acts*, *65*, 2379–2393.

Liu, Q., and R. A. Lange (2006), The partial molar volume of Fe_2O_3 in alkali silicate melts: Evidence for an average Fe^{3+} coordination number near five, *Am. Min.*, *91*(2–3), 385–393.

Liu, Q., R. A. Lange, and Y. H. Ai (2007), Acoustic velocity measurements on Na_2O-TiO_2-SiO_2 liquids: Evidence for a highly compressible TiO2 component related to five-coordinated Ti, *Geochim. Cosmochim. Acta*, *71*(17), 4314–4326, doi:10.1016/J.Gca.2007.06.054.

Luo, S. N., and T. J. Ahrens (2004), Shock-induced superheating and melting curves of geophysically important minerals, *Phys. Earth. Planet. Int.*, *143–144*, 369–386, doi:10.1016/j.pepi.2003.04.001.

Lyzenga, G. A., T. J. Ahrens, and A. C. Mitchell (1983), Shock temperatures of SiO_2 and their geophysical implications, *J. Geophys. Res.*, *88*, 2431–2444.

Matsukage, K. N., Z. C. Jing, and S. Karato (2005), Density of hydrous silicate melt at the conditions of Earth's deep upper mantle, *Nature*, *438*(7067), 488–491, doi:10.1038/Nature04241.

Mcqueen, R. G., S. P. Marsh, and J. N. Fritz (1967), Hugoniot equation of state of 12 rocks, *J. Geophys. Res.*, *72*(20), 4999.

Mibe, K., T. Fujii, A. Yasuda, and S. Ono (2006), Mg-Fe partitioning between olivine and ultramafic melts at high pressures, *Geochim. Cosmochim. Acta*, *70*(3), 757–766, doi:10.1016/j.gca.2005.09.022.

Miller, G. H., T. J. Ahrens, and E. M. Stolper (1988), The equation of state of molybdenum at 1400 °C, *J. Appl. Phys.*, *63*(9), 4469–4475.

Miller, G. H., E. M. Stolper, and T. J. Ahrens (1991), The equation of state of a molten komatiite, 1, Shock-wave compression to 36 GPa, *J. Geophys. Res.*, *96*(B7), 11831–11848.

Morbidelli, A. (2007), Impacts in the primordial history of terrestrial planets, *Comptes Rendus Geoscience*, *339*(14–15), 907–916, doi:10.1016/J.Crte.2007.09.001.

Mosenfelder, J. L., P. D. Asimow, and T. J. Ahrens (2007), Thermodynamic properties of Mg_2SiO_4 liquid at ultra-high pressure from shock measurements to 200 GPa on forsterite and wadsleyite, *J. Geophys. Res.*, *112*, B06208, doi:10.1029/2006JB004364.

Mosenfelder, J. L., P. D. Asimow, D. J. Frost, D. C. Rubie, and T. J. Ahrens (2009), The $MgSiO_3$ system at high pressure: Thermodynamic properties of perovskite, post-perovskite and melt from global inversion of shock and static compression data, *J. Geophys. Res.*, *114*, B01203, doi:10.1029/2008JB005900.

Murthy, V. R. (1992), Geochemical evidence for an initially molten Earth, *Phys. Earth. Planet. Int.*, *71*(1–2), 46–51.

Mysen, B. O., and P. Richet (2005), *Silicate Glasses and Melts: Properties and Structure*, 544 pp., Elsevier, Amsterdam.

Ohtani, E., Y. Nagata, A. Suzuki, and T. Kato (1995), Melting relations of peridotite and the density crossover in planetary mantles, *Chem. Geol.*, *120*(3–4), 207–221.

Petel, O. E., and F. X. Jette (2010), Comparison of methods for calculating the shock hugoniot of mixtures, *Shock Waves*, *20*(1), 73–83, doi:10.1007/S00193-009-0230-X.

Ricolleau, A., Y. W. Fei, E. Cottrell, H. Watson, L. W. Deng, L. Zhang, G. Fiquet, A. L. Auzende, M. Roskosz, G. Morard, and V. Prakapenka (2009), Density profile of pyrolite under the lower mantle conditions, *Geophys. Res. Lett.*, *36*, L06302, doi:10.1029/2008GL036759.

Rigden, S. M., T. J. Ahrens, and E. M. Stolper (1984), Densities of liquid silicates at high-pressures, *Science*, *226*(4678), 1071–1074.

Rigden, S. M., T. J. Ahrens, and E. M. Stolper (1988), Shock compression of molten silicate - results for a model basaltic composition, *J. Geophys. Res.*, *93*(B1), 367–382.

Rigden, S. M., T. J. Ahrens, and E. M. Stolper (1989), High-pressure equation of state of molten anorthite and diopside, *J. Geophys. Res.*, *94*(B7), 9508–9522.

Rivers, M. L., and I. S. E. Carmichael (1987), Ultrasonic studies of silicate melts, *J. Geophys. Res.*, *92*, 9247–9270.

Rost, S., E. J. Garnero, Q. Williams, and M. Manga (2005), Seismological constraints on a possible plume root at the core-mantle boundary, *Nature*, *435*(7042), 666–669.

Rost, S., E. J. Garnero, and Q. Williams (2006), Fine-scale ultralow-velocity zone structure from high-frequency seismic array data, *J. Geophys. Res.*, *111*, B09310, doi:10.1029/2005JB004088.

Rowan, L. R. (1993), Equation of state of molten mid-ocean ridge basalt. Structure of Kilauea volcano, Ph.D. thesis, 219 pp, California Institute of Technology, Pasadena.

Sakamaki, T., A. Suzuki, and E. Ohtani (2006), Stability of hydrous melt at the base of the Earth's upper mantle, *Nature*, *439*(7073), 192–194, doi:10.1038/Nature04352.

Sakamaki, T., E. Ohtani, S. Urakawa, A. Suzuki, and Y. Katayama (2009), Measurement of hydrous peridotite magma density at high pressure using the X-ray absorption method, *Earth Planet. Sci. Lett.*, *287*(3–4), 293–297, doi:10.1016/J.Epsl.2009.07.030.

Sakamaki, T., E. Ohtani, S. Urakawa, A. Suzuki, and Y. Katayama (2010), Density of dry peridotite magma at high pressure using an X-ray absorption method, *Am. Min.*, *95*(1), 144–147, doi:10.2138/Am.2010.3143.

Shearer, C. K., and J. J. Papike (1999), Magmatic evolution of the moon, *Am. Min.*, *84*(10), 1469–1494.

Spera, F. J., D. Nevins, M. Ghiorso, and I. Cutler (2009), Structure, thermodynamic and transport properties of $CaAl_2Si_2O_8$ liquid. Part I: Molecular dynamics simulations, *Geochim. Cosmochim. Acta*, *73*(22), 6918–6936, doi:10.1016/J.Gca.2009.08.011.

Stebbins, J. F., P. F. McMillan, and D. B. Dingwell (Eds.) (1995), *Structure, Dynamics, and Properties of Silicate Melts*, 616 pp., Mineralogical Society of America, Washington, D. C.

Steinberg, D. J. (1982), Some observations regarding the pressure dependence of the bulk modulus, *J. Phys. Chem. Solids*, *43*(12), 1173–1175.

Stixrude, L., and M. S. T. Bukowinski (1989), Compression of tetrahedrally bonded SiO_2 liquid and silicate liquid-crystal density inversion, *Geophys. Res. Lett.*, *16*(12), 1403–1406.

Stixrude, L., and B. Karki (2005), Structure and freezing of $MgSiO_3$ liquid in Earth's lower mantle, *Science*, *310*(5746), 297–299.

Stixrude, L., and C. Lithgow-Bertelloni (2005), Thermodynamics of mantle minerals - I. Physical properties, *Geophys. J. Int.*, *162*(2), 610–632.

Stixrude, L., N. de Koker, N. Sun, M. Mookherjee, and B. B. Karki (2009), Thermodynamics of silicate liquids in the deep Earth, *Earth Planet. Sci. Lett.*, *278*(3–4), 226–232, doi:10.1016/j.epsl.2008.12.006.

Stolper, E. M., D. Walker, B. H. Hager, and J. F. Hays (1981), Melt segregation from partially molten source regions: The importance of melt density and source region size, *J. Geophys. Res.*, *86*(B7), 6261–6271.

Stolper, E. M., and T. J. Ahrens (1987), On the nature of pressure-induced coordination changes in silicate melts and glasses, *Geophys. Res. Lett.*, *14*(12), 1231–1233.

Suzuki, A., E. Ohtani, and T. Kato (1998), Density and thermal expansion of a peridotite melt at high pressure, *Phys. Earth. Planet. Int.*, *107*(1–3), 53–61.

Svendsen, B., and T. J. Ahrens (1983), Dynamic compression of diopside and salite to 200 GPa, *Geophys. Res. Lett.*, *10*(7), 501–504.

Svendsen, B., and T. J. Ahrens (1990), Shock-induced temperatures of $CaMgSi_2O_6$, *J. Geophys. Res.*, *95*(B5), 6943–6953.

Tonks, W. B., and H. J. Melosh (1993), Magma ocean formation due to giant impacts, *J. Geophys. Res.*, *98*(E3), 5319–5333.

Trønnes, R. G., D. Canil, and K. J. Wei (1992), Element Partitioning between Silicate Minerals and Coexisting Melts at Pressures of 1–27 GPa, and Implications for Mantle Evolution, *Earth Planet. Sci. Lett.*, *111*(2–4), 241–255.

Walker, D., C. B. Agee, and Y. Zhang (1988), Fusion curve slope and crystal/liquid buoyancy, *J. Geophys. Res.*, *93*(B1), 313–323.

Williams, Q., R. Jeanloz, J. Bass, B. Svendsen, and T. J. Ahrens (1987), The melting curve of iron to 250 Gigapascals: A constraint on the temperature at Earth's center, *Science*, *236*, 181–182.

Wolf, G. H., and P. F. McMillan (1995), Pressure effects on silicate melt structure and properties, in *Structure, Dynamics and Properties of Silicate Melts*, edited by J. F. Stebbins et al., pp. 505–562, Mineralogical Society of America, Washington, D. C.

Xue, X. Y., J. F. Stebbins, M. Kanzaki, P. F. McMillan, and B. Poe (1991), Pressure-induced silicon coordination and tetrahedral structural-changes in Alkali Oxide-Silica melts up to 12 GPa - NMR, Raman, and infrared-spectroscopy, *Am. Min.*, *76*(1–2), 8–26.

T. J. Ahrens and P. D. Asimow, Division of Geological and Planetary Sciences, California Institute of Technology, 1200 E. California Blvd. M/C 170-25, Pasadena, CA 91125, USA. (asimow@gps.caltech.edu)